



**HAL**  
open science

## The Cyclic Imine Core Common to the Marine Macrocyclic Toxins Is Sufficient to Dictate Nicotinic Acetylcholine Receptor Antagonism

Yves Bourne, Gerlind Sulzenbacher, Laurent Chabaud, Rómulo Aráoz, Zoran Radić, Sandrine Conrod, Palmer Taylor, Catherine Guillou, Jordi Molgó,  
Pascale Marchot

► **To cite this version:**

Yves Bourne, Gerlind Sulzenbacher, Laurent Chabaud, Rómulo Aráoz, Zoran Radić, et al.. The Cyclic Imine Core Common to the Marine Macrocyclic Toxins Is Sufficient to Dictate Nicotinic Acetylcholine Receptor Antagonism. *Marine drugs*, 2024, *Marine Biotoxins 2.0*, 22 (4), pp.149. 10.3390/md22040149 . hal-04542228

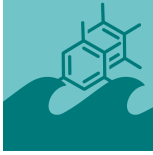
**HAL Id: hal-04542228**

**<https://hal.science/hal-04542228>**

Submitted on 11 Apr 2024

**HAL** is a multi-disciplinary open access archive for the deposit and dissemination of scientific research documents, whether they are published or not. The documents may come from teaching and research institutions in France or abroad, or from public or private research centers.

L'archive ouverte pluridisciplinaire **HAL**, est destinée au dépôt et à la diffusion de documents scientifiques de niveau recherche, publiés ou non, émanant des établissements d'enseignement et de recherche français ou étrangers, des laboratoires publics ou privés.



Article

---

# The Cyclic Imine Core Common to the Marine Macrocyclic Toxins Is Sufficient to Dictate Nicotinic Acetylcholine Receptor Antagonism

---

Yves Bourne, Gerlind Sulzenbacher, Laurent Chabaud, Rómulo Aráoz, Zoran Radić, Sandrine Conrod, Palmer Taylor, Catherine Guillou, Jordi Molgó and Pascale Marchot

## Special Issue






Marine Biotoxins 2.0

Edited by  
Prof. Dr. Jordi Molgó



## Article

# The Cyclic Imine Core Common to the Marine Macrocyclic Toxins Is Sufficient to Dictate Nicotinic Acetylcholine Receptor Antagonism

Yves Bourne<sup>1</sup>, Gerlind Sulzenbacher<sup>1</sup>, Laurent Chabaud<sup>2,†</sup>, Rómulo Aráoz<sup>3</sup>, Zoran Radić<sup>4</sup>, Sandrine Conrod<sup>5,‡</sup>, Palmer Taylor<sup>4</sup>, Catherine Guillou<sup>2</sup>, Jordi Molgó<sup>3</sup> and Pascale Marchot<sup>1,5,\*</sup>

- <sup>1</sup> Lab "Architecture et Fonction des Macromolécules Biologiques" (AFMB), Aix-Marseille Univ, CNRS, Faculté des Sciences Campus Luminy, 13288 Marseille cedex 09, France; yves.bourne@univ-amu.fr (Y.B.); gerlind.sulzenbacher@univ-amu.fr (G.S.)
- <sup>2</sup> Institut de Chimie des Substances Naturelles (ICSN), Univ Paris-Saclay, CNRS, 91198 Gif-sur-Yvette, France; catherine.guillou@cnrs.fr (C.G.)
- <sup>3</sup> Service d'Ingénierie Moléculaire pour la Santé (SIMoS) EMR CNRS 9004, Département Médicaments et Technologies pour la Santé, Institut des Sciences du Vivant Frédéric Joliot, CEA, INRAE, Université Paris-Saclay, 91191 Gif-sur-Yvette, France; romulo.araoz@cea.fr (R.A.); jordi.molgo@cea.fr (J.M.)
- <sup>4</sup> Skaggs School of Pharmacy and Pharmaceutical Sciences (SSPPS), University of California San Diego, La Jolla, CA 92093-0751, USA; zradic@health.ucsd.edu (Z.R.); pwtaylor@health.ucsd.edu (P.T.)
- <sup>5</sup> Centre de Recherche en Neurobiologie et Neurophysiologie de Marseille (CRN2M), Aix Marseille Univ, CNRS, 13344 Marseille, France
- \* Correspondence: pascale.marchot@univ-amu.fr
- † Current address: Institut des Sciences Moléculaires (ISM), Univ Bordeaux, CNRS, Bordeaux INP, 33400 Talence, France; laurent.chabaud@u-bordeaux.fr
- ‡ Current address: CEREGE, Aix-Marseille Univ, CNRS, IRD, Collège de France, INRAE, 13545 Aix-en-Provence, France; conrod@cerege.fr



**Citation:** Bourne, Y.; Sulzenbacher, G.; Chabaud, L.; Aráoz, R.; Radić, Z.; Conrod, S.; Taylor, P.; Guillou, C.; Molgó, J.; Marchot, P. The Cyclic Imine Core Common to the Marine Macrocyclic Toxins Is Sufficient to Dictate Nicotinic Acetylcholine Receptor Antagonism. *Mar. Drugs* **2024**, *22*, 149. <https://doi.org/10.3390/md22040149>

Academic Editor: David Adams

Received: 13 February 2024

Revised: 22 March 2024

Accepted: 25 March 2024

Published: 27 March 2024



**Copyright:** © 2024 by the authors. Licensee MDPI, Basel, Switzerland. This article is an open access article distributed under the terms and conditions of the Creative Commons Attribution (CC BY) license (<https://creativecommons.org/licenses/by/4.0/>).

**Abstract:** Macrocyclic imine phycotoxins are an emerging class of chemical compounds associated with harmful algal blooms and shellfish toxicity. Earlier binding and electrophysiology experiments on nAChR subtypes and their soluble AChBP surrogates evidenced common trends for substantial antagonism, binding affinities, and receptor-subtype selectivity. Earlier, complementary crystal structures of AChBP complexes showed that common determinants within the binding nest at each subunit interface confer high-affinity toxin binding, while distinctive determinants from the flexible loop C, and either capping the nest or extending toward peripheral subsites, dictate broad versus narrow receptor subtype selectivity. From these data, small spiroimine enantiomers mimicking the functional core motif of phycotoxins were chemically synthesized and characterized. Voltage-clamp analyses involving three nAChR subtypes revealed preserved antagonism for both enantiomers, despite lower subtype specificity and binding affinities associated with faster reversibility compared with their macrocyclic relatives. Binding and structural analyses involving two AChBPs pointed to modest affinities and positional variability of the spiroimines, along with a range of AChBP loop-C conformations denoting a prevalence of antagonistic properties. These data highlight the major contribution of the spiroimine core to binding within the nAChR nest and confirm the need for an extended interaction network as established by the macrocyclic toxins to define high affinities and marked subtype specificity. This study identifies a minimal set of functional pharmacophores and binding determinants as templates for designing new antagonists targeting disease-associated nAChR subtypes.

**Keywords:** acetylcholine-binding protein; binding affinity; competitive antagonism; crystal structure; cyclic imine; electrophysiology; nicotinic acetylcholine receptor; pharmacophore; receptor subtype selectivity; spiroimine

## 1. Introduction

Cyclic imine toxins are a globally distributed and emerging family of marine macrocyclic biotoxins comprising seven different main groups of low-molecular-weight organic compounds: the gymnodimines, spirolides, pinnatoxins, pteriatoxins, portimines, prorocontrolides, and spiroprorocentrimine (for reviews, see [1–5]). Even though most of the discovered toxins with a characteristic cyclic imine function were found primarily in shellfish, most of the available evidence strongly indicates that marine dinoflagellates are responsible for the production of cyclic imine toxins. These lipophilic toxins as well as a large number of acyl derivative products of shellfish metabolism [6–11] can bioaccumulate and contaminate filter-feeding (bivalves) edible mollusks and other marine invertebrate species [12]. Therefore, they represent a risk for shellfish consumers (for reviews, see [13,14]), especially since some emerging cyclic imine toxins have the ability to cross the intestinal, blood–brain, and placental barriers [15].

The *Karenia selliformis* dinoflagellate produces gymnodimines A–C [16–20], while 12-methyl gymnodimine-A, 12-methyl gymnodimine-B, gymnodimine-D, and 16-desmethyl gymnodimine-D are produced by the dinoflagellate *Alexandrium ostenfeldii* [21–26]. The use of liquid chromatography-high resolution mass spectrometry has considerably expanded the number of known gymnodimine congeners (gymnodimines F–J) [11]. The dinoflagellate *A. ostenfeldii* has primarily been associated with the production of spirolides [27,28], which constitute the largest and most highly diverse group among the cyclic imine toxins [29–32]. The cosmopolitan benthic dinoflagellate *Vulcanodinium rugosum* [33–35] is the producer of pinnatoxins [36–38], portimines A and B [39,40], and kabirimine [41]. Pteriatoxins A–C, first isolated from the Okinawan oyster *Pteria penguin* [42], are supposed to be shellfish metabolites of a cyclic imine toxin precursor [43]. The dinoflagellate origin of pteriatoxins remains to be determined. Finally, *Prorocentrum lima* and *P. maculosum* have been related to the biosynthesis of prorocontrolides A and B, respectively [44–46], of which three analogs, prorocontrolide C and 4-hydroxyprorocontrolide from the benthic dinoflagellate *P. lima* [47], and spiro-prorocentrimine from a benthic *Prorocentrum* sp. of Taiwan [30,48], were also isolated.

The chemical structures of the cyclic imine toxins exhibit a rich diversity involving a macrocyclic ring (14 to 27 carbon atoms) and two constant moieties: the cyclic imine (mostly found as a spiroimine) and the spiroketal ring system. In prorocontrolides, the 26-membered carbo-macrocyclic lactone is arranged around a hexahydroisoquinoline that incorporates the cyclic imine group [43,44]. In turn, the cyclic imines are composed of 5-membered (portimines), 6-membered (gymnodimines, spiroprorocentrimine, prorocontrolides, and kabirimine), or 7-membered rings (spirolides, pinnatoxins, pteriatoxins). The other structural constituents of the ring system are one or two tetrahydrofurans (in portimine and gymnodimine A, and in gymnodimine D, respectively), or a tetrahydropyran (in prorocontrolides and spiroprorocentrimine), or more complex 6,5-(spirolides H and I), 6,6,5-(spirolide G), 6,5,5-(spirolides A–F), or 6,5,6-spiroketal moieties (in pinnatoxins and pteriatoxins) (for reviews, see [3,30,49]).

Most, if not all, of these toxins have been identified as competitive antagonists of the nicotinic acetylcholine receptors (nAChRs), initially from the central neurological symptoms and rapid lethality that they induced in mice, and then through the recording of nicotinic currents from various nAChR subtypes (for reviews, see [3,50,51]). The nAChRs are prototypical cation-selective, ligand-gated ion channels (LGIC) that mediate fast neurotransmission in the central and peripheral nervous systems [52,53]. They belong to the Cys-loop subfamily of LGICs and are formed by distinct combinations of five subunits that confer selectivity in pharmacological properties and regional tissue locations. In mammals, the diversity in the nAChR subunit subtypes and assemblies is most evident in the central nervous system, where up to nine  $\alpha$  and three  $\beta$  subunits have been described, of which some can arrange as homopentamers with five acetylcholine (ACh)-binding sites (e.g.,  $\alpha 7$  and  $\alpha 9$  subtypes) or as heteropentamers of two different subunits with either two or three ACh-binding sites (e.g.,  $\alpha 3\beta 2$  and  $\alpha 4\beta 2$  subtypes) [54–56]. An additional

level of complexity arises from the assembly of four distinct subunits in the muscle-type nAChR,  $\alpha_1\beta_2\gamma\delta$  [54,56]. The various nAChRs used in this study are further described in Appendix A, and their subunit sequences are displayed in Figure A1.

During the last decade, an impressive number of medium- to high-resolution structures of several full-length LGICs in the absence or presence of bound ligands have been solved by X-ray crystallography or cryo-electron microscopy (EM) (for reviews, see [55–58]) including those of the  $\alpha_7$  [59],  $\alpha_4\beta_2$  [60], and  $\alpha_1\beta_2\gamma\delta$  nAChR subtypes [61]. These structures provided fundamental insights into the gating mechanisms of LGICs. However, despite the remarkable technological and experimental progress, using full-length receptors for identifying the molecular determinants involved in agonist and competitive antagonist binding remains both time and cost consuming, and risky in terms of success.

The soluble ACh-binding proteins (AChBP) from mollusks form homopentameric assemblies of subunits homologous to the N-terminal, extracellular ligand binding domain (LBD) of the nAChR [62–64] (Figure A1). In addition to the overall structural features of the subunits, the aromatic side chains that form the ligand-binding pocket at the subunit interfaces are well conserved in the nAChR family, with greater variability for residues at the complementary or (–) face than the principal or (+) face of each interface. The binding pocket of AChBP possesses all of the functional residues identified in the nAChR LBD, and its extension toward various directions of the interface provides multiple means for selective accommodation of the nicotinic ligands [63–68]. Overall, nicotinic full and partial agonists recognize the “core agonist signature motif” central to the binding pocket and capped by loop C, located on the (+) face, whereas the larger competitive antagonists also extend toward peripheral directions along the interface, resulting in the opening of loop C and often in greater subtype selectivity than seen for agonists (for recent reviews, see [69,70]). However, AChBPs are devoid of the transmembrane domains and intracellular loops typical for nAChRs, and hence, of the capacity of conducting ions and mediating neurotransmission.

Previously, we documented the parameters and mode of binding of two pairs of closely related macrocyclic imine toxins, 13-desmethyl spiroside C (SPX) and (–)-gymnodimine-A (GYM) [71], and pinnatoxins A (PnTxA) and G (PnTxG) [72] (Figure 1) to several representative nAChR subtypes and two AChBP subtypes. Our data identified the molecular determinants on both the toxins and receptors dictating potent nicotinic antagonism. They also identified those responsible for the broad selectivity of SPX and GYM toward the various nAChR subtypes, and for the narrow selectivity of the pinnatoxins toward the muscle-type  $\alpha_1\beta_2\gamma\delta$  or neuronal  $\alpha_7$  nAChR subtypes *versus* the neuronal  $\alpha_3\beta_2$  and  $\alpha_4\beta_2$  nAChRs. In particular, we showed that affinity is dictated by the protonated imine nitrogen common to the macrocyclic toxins, while specificity is imposed by toxin determinants extending out of the agonist-binding nest toward apical, radial, or ‘membrane’ sides of the LBD. Since peptidic neurotoxins acting as subtype-selective nAChR antagonists (e.g., curarimimetic  $\alpha$ -neurotoxin, waglerins,  $\alpha$ -conotoxins) are polar molecules unable to cross the blood–brain barrier, we propose that the lipophilic macrocyclic imine framework might offer new avenues for distinguishing nAChR subtype functions in the brain.

A synthetic tetrahydrofuran fragment mimicking the C10–C20 skeleton of GYM was found not to bind the  $\alpha_1\beta_2\gamma\delta$  nAChR [73]. In contrast, a series of small synthetic analogs of its 6,6-spiroimine core were found to inhibit ACh-evoked nicotinic currents on the  $\alpha_4\beta_2$  and  $\alpha_1\beta_2\gamma\delta$  nAChR subtypes, although they were much less active than the parental phycotoxin. These data revealed that the spiroimine moiety is critical for the blockade of nAChRs and pointed to it as a possible pharmacophore of this group of toxins [74]. To confirm the identity of the minimal core motif dictating nAChR antagonism, we then synthesized a new analog of 6,6-spiroimine, differing from the previous ones through incorporation of a dioxolane moiety. This molecule was first generated as a ( $\pm$ ) racemate and named “spiroimine” [75].

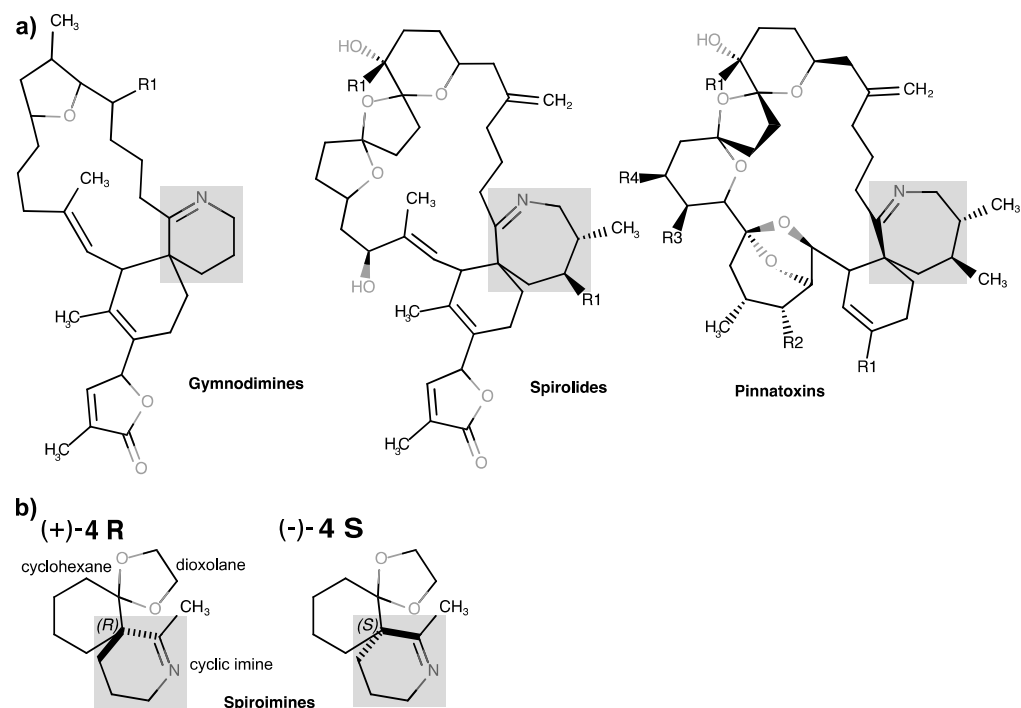


**Figure 1.** Chemical structures of the gymnodimine, spirolide, and pinnatoxin variants sharing a spiroimine core, and of the spiroimine enantiomers synthesized in this study. (a) The 6- or 7-membered cyclic imines are highlighted with a gray background. The spiroketal ring system is at the top of the macrocyclic ring. Locations of group substitutions (R1 to R4) that differ among the variants are indicated. (b) Spiroimines (+)-4 R and (-)-4 S with their chiral center and ring systems labeled.

Here, from this racemic spiroimine, we purified and characterized the two enantiomers, (+) R and (−) S, and carried out a comprehensive study of their mode of action by recording voltage-clamp currents from the muscle-type  $\alpha_1\alpha_2\beta\gamma\delta$  and neuronal  $\alpha 7$  and  $\alpha 4\beta 2$  nAChRs along with binding parameters on AChBPs from *Aplysia californica* (A-AChBP) and *Lymnaea stagnalis* (L-AChBP), and by solving X-ray structures of their A-AChBP complexes. This study identified a minimal set of functional determinants and binding sites as a framework for the design of new effectors targeting disease-associated nAChR subtypes.

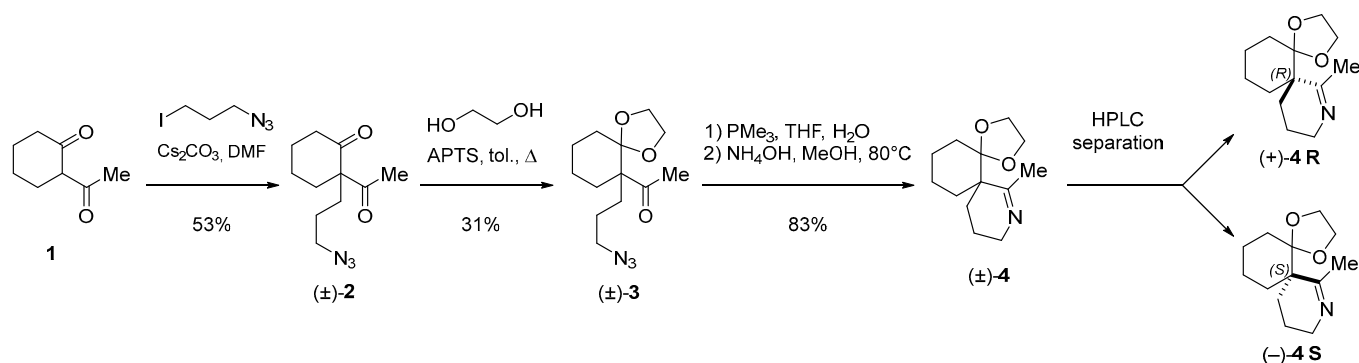
## 2. Results and Discussion

### 2.1. Chemical Synthesis and Characterization of the Spiroimine Enantiomers

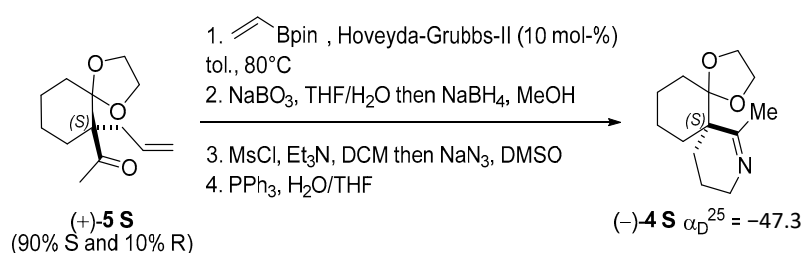
The spiroimine ( $\pm$ )-4 racemate was synthesized in three steps from diketone **1** using standard procedures (Scheme 1; Appendix B). Separation by chiral HPLC of the two enantiomers present in ( $\pm$ )-4 yielded virtually pure spiroimines (+)-4 and (−)-4.

To assign the absolute configuration of the enantiopure spiroimines, (−)-4 was also synthesized from ketone (+)-5 S, prepared according to [76]. Spiroimine (−)-4 was found to have configuration S at the quaternary carbon (Scheme 2; Appendix B), and hence, spiroimine (+)-4 was considered to be of the opposite configuration R. The two enantiomers were therefore designated as (+)-4 R and (−)-4 S.

Initial electrophysiology experiments on nAChRs and binding and crystallography experiments on AChBPs were carried out using the racemic spiroimine ( $\pm$ )-4. These were then complemented by more comprehensive experiments performed with the enantiopure spiroimines (+)-4 R and (−)-4 S.



**Scheme 1.** Racemic synthesis of spiroimine ( $\pm$ )-4 and separation of the (+)-4 and (−)-4 enantiomers. The yield at each step is indicated.



**Scheme 2.** Determination of the absolute configuration of (−)-4 S.

## 2.2. Functional Characteristics and nAChR Subtype Selectivity of the Spiroimine Racemate and Enantiomers

Functional analysis of the ( $\pm$ )-4 racemate and (+)-4 R and (−)-4 S enantiomers used either manual or automated two-electrode voltage-clamp (TEVC) recordings on *Xenopus laevis* oocytes at  $-60$  mV holding membrane potential. The oocytes were either micro-transplanted with *Torpedo*  $\alpha 1_2\beta\gamma\delta$ -enriched electrocyte membranes or transfected with human  $\alpha 7$  or  $\alpha 4\beta 2$ -encoding cDNAs. When applied alone (see *Experimental Procedures*), none of the three spiroimines induced nAChR channel opening, thereby discarding any agonistic activity toward these nAChR subtypes. Instead, when applied together with ACh at its  $EC_{50}$  concentration for each nAChR subtype, all three spiroimines clearly behaved as nicotinic antagonists, whose potency depended on the receptor subtype examined (Figure 2; Table 1).

**Table 1.** Inhibition constants ( $IC_{50}$  values) for the effect of the spiroimines on ACh-evoked nicotinic currents recorded from oocytes either transplanted with the *Torpedo* muscle-type  $\alpha 1_2\beta\gamma\delta$  nAChR or expressing the human neuronal  $\alpha 7$  or  $\alpha 4\beta 2$  nAChRs.

nAChR Subtype	$IC_{50}$ ( $\mu$ M) <sup>a</sup> and Hill Slope <sup>b</sup>		
	Racemic ( $\pm$ )-4	Spiroimine (+)-4 R	Spiroimine (−)-4 S
<i>Torpedo</i> $\alpha 1_2\beta\gamma\delta$	0.24 (0.19–0.26) <sup>a</sup> $\sim 1$ <sup>b</sup>	0.37 (0.29–0.47) <sup>a</sup> $\sim 1$ <sup>b</sup>	0.33 (0.18–0.61) <sup>a</sup> $\sim 1$ <sup>b</sup>
Human $\alpha 7$	2.11 (1.39–3.21) <sup>a</sup> 0.61 (0.47–0.75) <sup>b</sup>	4.88 (3.16–7.51) <sup>a</sup> 0.78 (0.54–1.01) <sup>b</sup>	1.45 (0.89–2.36) <sup>a</sup> 0.58 (0.44–0.72) <sup>b</sup>
Human $\alpha 4\beta 2$	6.96 (5.77–8.39) <sup>a</sup> 1.08 (0.86–1.29) <sup>b</sup>	9.31 (3.26–26.59) <sup>a</sup> 0.83 (0.15–1.52) <sup>b</sup>	1.41 (0.63–3.15) <sup>a</sup> 0.53 (0.32–0.74) <sup>b</sup>

<sup>a,b</sup> Values from individual experiments performed in triplicate or quadruplicate with the 95% confidence intervals provided in parentheses. The experimental curves associated with these data are reported in Figure 2.

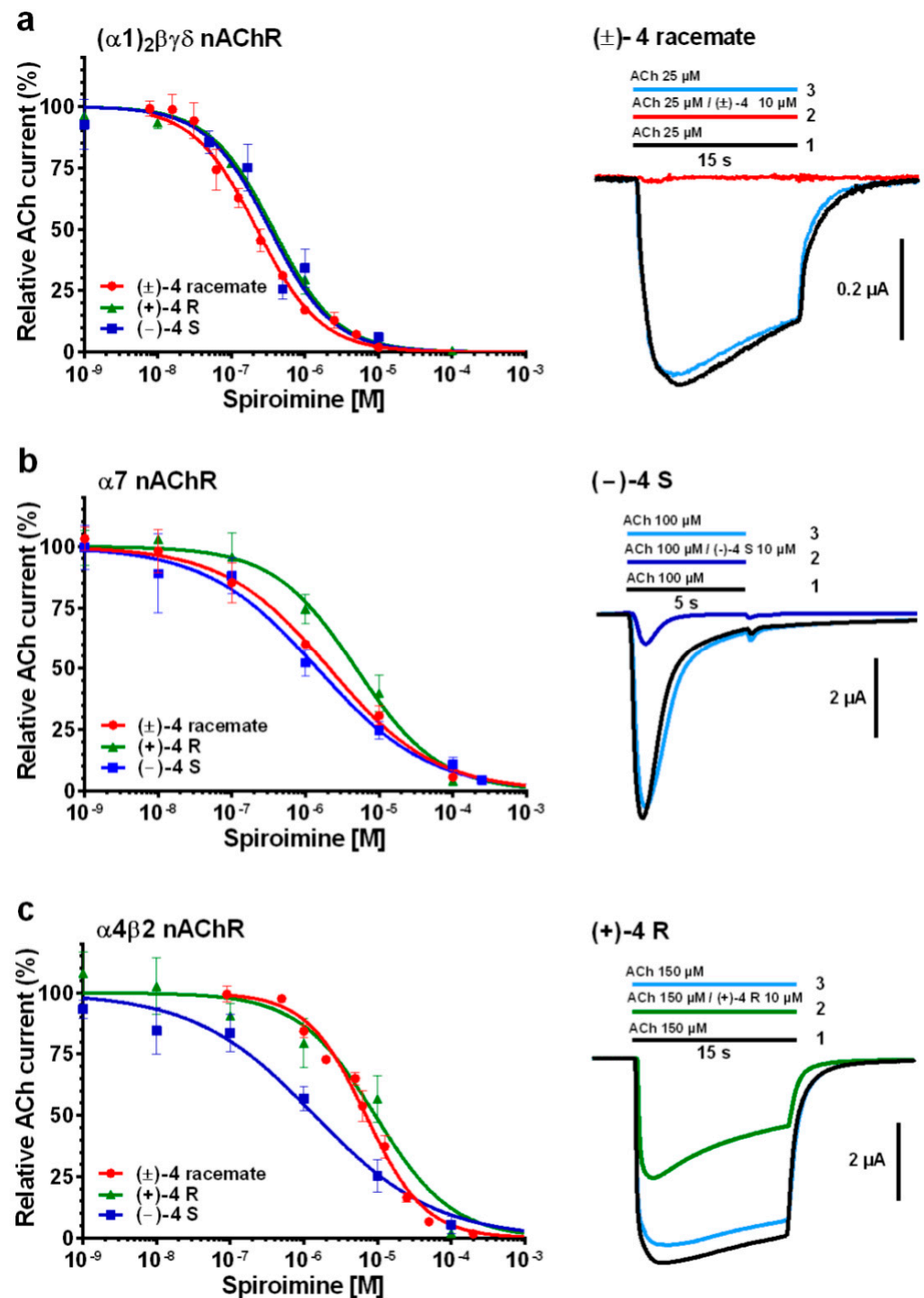


**Figure 2.** Competitive antagonism of *Torpedo* muscle-type and human neuronal nAChR subtypes by the spiroimines. (a) *Left*: Concentration-dependent inhibition of IACH peak amplitude in  $\alpha_1_2\beta\gamma\delta$  nAChR by the (±)-4 racemate (red curve) and the (+)-4 R (green curve) and (-)-4 S enantiomers (blue curve). *Right*: Superimposed nicotinic currents evoked by perfusing an oocyte with ACh alone (25  $\mu$ M, 15 s, control black tracing 1), then with a mix of ACh and (±)-4 racemate (25  $\mu$ M and 10  $\mu$ M [i.e., 45-fold the  $IC_{50}$  of the racemate for  $\alpha_1_2\beta\gamma\delta$ , see Table 1] respectively, 15 s, red tracing 2), and after a 210 s wash with Ringer's solution, again with ACh (25  $\mu$ M, 15 s, light blue tracing 3) [representative data]. (b) *Left*: Concentration-dependent inhibition of IACH peak amplitude in  $\alpha_7$  nAChR by the three spiroimines [same color codes as in left panel (a)]. *Right*: Superimposed inward currents elicited by perfusing an oocyte with ACh alone (100  $\mu$ M, 5 s, control black tracing 1), then with a mix of ACh



and enantiomer (–)-4 S (100  $\mu$ M and 10  $\mu$ M [i.e., 7-fold the  $IC_{50}$  of (–)-4 S for  $\alpha 7$ ] respectively, 5 s, dark blue tracing 2), and after a 210 s wash with Ringer’s solution, again with ACh (100  $\mu$ M, 5 s, light blue tracing 3). (c) *Left*: Concentration-dependent inhibition of IACH peak amplitude in  $\alpha 4\beta 2$  nAChR by the three spiroimines [same color codes as in left panels (a,b)]. *Right*: Superimposed ACh-currents evoked by perfusing an oocyte with ACh alone (150  $\mu$ M, 30 s, control black tracing 1), then with a mix of ACh and enantiomer (+)-4 R (150  $\mu$ M and 10  $\mu$ M [i.e., 3-fold the  $IC_{50}$  of (+)-4 R for  $\alpha 4\beta 2$ ], respectively, 15 s, green tracing 2), and after a 210 s wash with Ringer’s solution, again with ACh (150  $\mu$ M, 15 s, light blue tracing 3). The  $IC_{50}$  values and confidence intervals calculated from these data are reported in Table 1.

Indeed, the concentration–response curves recorded on the  $\alpha 1_2\beta\gamma\delta$  nAChR showed a full antagonistic effect at high spiroimine concentration, with  $IC_{50}$  values in the *low*  $\mu$ M range for the three spiroimines, with no stereospecificity and no apparent cooperativity or difference in the binding affinities to the  $\alpha\gamma$  and  $\alpha\delta$  interfaces (Figure 2a left; Table 1). Perfusion of a mixed ACh/spiroimine solution markedly inhibited the ACh-evoked current (IACH), as here exemplified with the ( $\pm$ )-4 racemate (Figure 2a right, tracing 2). When the  $\alpha 1_2\beta\gamma\delta$  nAChR was in the desensitized state, the washout of the bound spiroimine with ACh triggered the immediate reopening of the receptor channel and full recovery of the nicotinic current up to the amplitude level of the control desensitized state, a feature denoting fast reversibility of channel blockade by the spiroimine (Figure 2a right, tracing 3).

Concentration–response curves recorded on the  $\alpha 7$  nAChR also showed a full antagonistic effect at high spiroimine concentration, with  $IC_{50}$  values in the *medium*  $\mu$ M range, and slightly higher, albeit not statistically different, for the (+)-4 R enantiomer compared to its two relatives (Figure 2b left; Table 1). Unexpectedly, negative cooperativity was observed, higher for the (–)-4 S enantiomer than the (+)-4 R enantiomer, and averaged for the ( $\pm$ )-4 racemate, suggesting the contribution of an allosteric component to  $\alpha 7$  antagonism by the spiroimines along with stereospecific modes of binding. Here again, recovery of the ACh-evoked current following the washout of bound spiroimine was fast and complete, as here exemplified with enantiomer (–)-4 S (Figure 2b right, tracing 3).

Similar antagonistic potency trends were again obtained for the  $\alpha 4\beta 2$  nAChR, with  $IC_{50}$  values in the *medium-to-high*  $\mu$ M range, but now significantly higher, by ca. one order of magnitude, for both the ( $\pm$ )-4 racemate and (+)-4 R enantiomer compared to their (–)-4 S relative (Figure 2c left; Table 1). Here again, negative cooperativity was observed, higher for the more potent (–)-4 S enantiomer than for the (+)-4 R enantiomer and ( $\pm$ )-4 racemate. Recovery of the ACh-evoked current was fast and complete, as here exemplified with enantiomer (+)-4 R (Figure 2c right, tracing 3; Figure 3a) and with the ( $\pm$ )-4 racemate using a slightly different protocol (Figure 3b).

Overall, these data point to similar antagonistic potencies of the three spiroimines for the muscle-type  $\alpha 1_2\beta\gamma\delta$  nAChR and a slightly higher potency of the (–)-4 S enantiomer for the neuronal  $\alpha 7$  and  $\alpha 4\beta 2$  nAChR subtypes compared to its two relatives, with a one order of magnitude stereospecificity for  $\alpha 4\beta 2$ . However, they also point to a higher selectivity, by 13- and 25-fold, of the (+)-4 R enantiomer for the  $\alpha 1_2\beta\gamma\delta$  nAChR compared with the  $\alpha 7$  and  $\alpha 4\beta 2$  subtypes. The  $IC_{50}$  values recorded for the ( $\pm$ )-4 racemate were overall consistent with the presence of the two enantiomers in a 1:1 ratio (see *Experimental Procedures*).

These data also support the role of the spiroimine moiety in the cyclic imine toxins as a main pharmacophore, as previously approached using 6,6-spiroimine analogs of GYM [74], whereas a synthetic tetrahydrofuran fragment mimicking the C10–C20 skeleton of GYM was found not to bind the  $\alpha 1_2\beta\gamma\delta$  nAChR [73]. Hence, developing spiroimine-like bioactive molecules may be a promising strategy for designing new effectors targeting disease-associated nAChR subtypes. In turn, the weak antagonistic potency of the spiroimines, lower than that of GYM by two ( $\alpha 1_2\beta\gamma\delta$ ) to three ( $\alpha 7$ ) to four ( $\alpha 4\beta 2$ ) orders of magnitude [71,77], likely proceeds from a much shorter residence time (i.e., greater  $k_{off}$  value) within the orthosteric binding site of the nAChRs due to the limited number of possible interactions with the subunit interface enabled by their small molecular size. Competition binding studies on nAChRs expressed at the surface of mammalian cells were

not performed; however, these parameters were explored through binding studies on A- and L-AChBP and the structural analysis of spiroimine-A-AChBP complexes (see below).

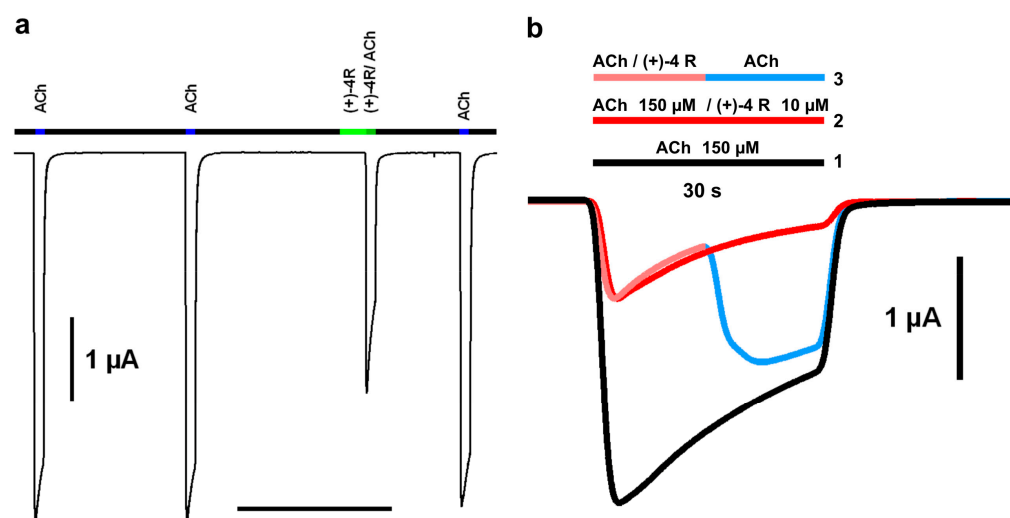


**Figure 3.** Typical nicotinic current recordings and effect of the (+)-4 R enantiomer and (±)-4 racemate on the  $\alpha 4\beta 2$  nAChR. (a) Two control inward currents were evoked by successive ACh pulses (150  $\mu$ M, 15 s, blue lines) with an intermediate 120 s wash using standard medium. After another 120 s wash, the oocyte was perfused with enantiomer (+)-4 R alone (10  $\mu$ M, 30 s, light green line), which elicited no inward current per se. Subsequent perfusion with a mix of ACh and (+)-4 R (150  $\mu$ M and 10  $\mu$ M, respectively, 15 s, dark green line) elicited a reduced nicotinic inward current compared to the controls. After a 90 s wash, recovery of the initial current amplitude was ascertained by repeating the control ACh perfusion (blue line). Horizontal calibration: 120 s. (b) Superimposed inward currents evoked by perfusing an oocyte with ACh (150  $\mu$ M, 30 s, control black tracing 1), then with a mix of ACh and (±)-4 racemate (150  $\mu$ M and 10  $\mu$ M, respectively, 30 s, red tracing 2), and then with the same ACh/racemate mix (15 s, pink tracing 3) immediately followed by ACh alone (150  $\mu$ M, 15 s, light blue tracing 3). Note the fast reversibility of the (±)-4 racemate.

### 2.3. Binding Characteristics of the Spiroimine Enantiomers toward A- and L-AChBPs

The sequence differences and distinctive binding affinities of A- and L-AChBP for nicotinic ligands render them useful templates for approaching ligand binding to various nAChR subtypes. These differences are exemplified by the A-AChBP lower affinity for ACh, but higher affinity for some  $\alpha 7$ -specific peptidic antagonists, a feature that renders it more “ $\alpha 7$ -like” than L-AChBP [63,64,69,70].

Equilibrium dissociation constants were determined either from ratios ( $K_d/(k_{off}/k_{on})$ ) of rate constants determined using multiple kinetic means ( $k_{on}$ ,  $k_{off}$ ,  $k_{off}/GAL$ ) or directly from stopped-flow measurements ( $K_d/SF_{eq}$ ,  $K_d/SPA_{eq}$ ) (see *Experimental Procedures*). Overall, interaction of the spiroimines with each AChBP was found to be clearly stereospecific (Table 2). Specificity was even more pronounced with L-AChBP with a one-to-two orders of magnitude difference between the equilibrium constants ( $K_d$  values) of the (+)-4 R and (−)-4 S enantiomers. This difference most likely arises from the slower association (lower  $k_{on}$  values) and faster dissociation (higher  $k_{off}$  value) of enantiomer (+)-4 R, as also suggested by the kinetic values obtained for racemic (±)-4 and reflected in the fraction of the complex too low for reliable detection under the experimental conditions of the stopped-flow measurement. Enantiomer (+)-4 R was a tighter binder to A-AChBP, albeit with a modest stereospecificity of up to two-fold arising largely from slower complex dissociation (lower  $k_{off}$  values). In turn, enantiomer (−)-4 S bound tighter to L-AChBP with  $K_d$  values in the  $10^{-7}$  M range, resulting in the tightest complex of all combinations, while enantiomer (+)-4 R bound with  $K_d$  values in the  $10^{-5}$  M range, not permitting the separation of rate constants for complex formation and dissociation under pre-equilibrium conditions.

**Table 2.** Kinetic constants for association ( $k_{on}$ ) and dissociation ( $k_{off}$  and  $k_{off}/GAL$ ) and equilibrium dissociation constants ( $K_d/(k_{off}/k_{on})$ ,  $K_d/SF_{eq}$ ,  $K_d/SPA_{eq}$ ) for spiroimine binding to purified AChBPs.

AChBP Subtype	Kinetic/Equilibrium Parameters	Racemic ( $\pm$ )-4	Spiroimine (+)-4 R	Spiroimine (–)-4 S
L-AChBP	$k_{on}$ ( $10^9 M^{-1} min^{-1}$ ) <sup>a</sup>	$3.6 \pm 0.6$	n.d.	$7.8 \pm 0.1$
	$k_{off}$ ( $10^3 min^{-1}$ ) <sup>a</sup>	$6.2 \pm 1.6$	n.d.	$3.2 \pm 1.1$
	$k_{off}/GAL$ ( $10^3 min^{-1}$ ) <sup>a</sup>	$6.7 \pm 0.6$	n.d.	$6.2 \pm 0.1$
	$K_d/(k_{off}/k_{on})$ ( $\mu M$ ) <sup>b</sup>	1.7	n.a.	0.41
	$K_d/SF_{eq}$ ( $\mu M$ ) <sup>c</sup>	$0.32/15^d$	12	0.32
	$K_d/SPA_{eq}$ ( $\mu M$ ) <sup>a</sup>	$2.6 \pm 1.9$	$12 \pm 3$	$(3.4 \pm 0.3)^e$
A-AChBP	$k_{on}$ ( $10^9 M^{-1} min^{-1}$ ) <sup>a</sup>	$6.3 \pm 1.2$	$7.4 \pm 0.4$	$6.1 \pm 0$
	$k_{off}$ ( $10^3 min^{-1}$ ) <sup>a</sup>	$18 \pm 2$	$16 \pm 1$	$26 \pm 1$
	$k_{off}/GAL$ ( $10^3 min^{-1}$ ) <sup>a</sup>	$15 \pm 0$	$14 \pm 1$	$24 \pm 1$
	$K_d/(k_{off}/k_{on})$ ( $\mu M$ ) <sup>b</sup>	2.9	2.2	4.3
	$K_d/SF_{eq}$ ( $\mu M$ ) <sup>c</sup>	4.2	3.1	5.4
	$K_d/SPA_{eq}$ ( $\mu M$ ) <sup>a</sup>	$2.4 \pm 1.5$	$2.3 \pm 0.4$	$2.4 \pm 0.5$

<sup>a</sup> Average  $\pm$  the variation ( $n = 2$ ) or mean  $\pm$  SD ( $n > 2$ ) of distinct experiments performed in triplicate. <sup>b</sup> Calculated from the rate constants. <sup>c</sup> Single value from a single experiment performed in triplicate. <sup>d</sup> Two constants issued from a biphasic curve. <sup>e</sup> Divergent value relative to other approaches. n.d., not detectable. n.a., not applicable. For definitions of  $k_{off}/GAL$ ,  $K_d/(k_{off}/k_{on})$ ,  $K_d/SF_{eq}$ ,  $K_d/SPA_{eq}$ , please refer to Section 3.3. in the *Experimental Procedures*.

The interaction constant values determined by the different experimental approaches generally agreed well (Table 2). Both the  $k_{off}$  and  $k_{off}/GAL$  values and the  $K_d/(k_{off}/k_{on})$ ,  $K_d/SF_{eq}$  and  $K_d/SPA_{eq}$  values determined in differently designed assays were comparable. Only the  $K_d/SPA_{eq}$  value determined for enantiomer (–)-4 S binding to L-AChBP was ca. one order of magnitude higher than the  $K_d/(k_{off}/k_{on})$  and  $K_d/SF_{eq}$  values determined in two different stopped-flow based assays (performed under pre-equilibrium and equilibrium conditions of spiroimine interaction to AChBP). Hence, this divergent value may have to be considered with caution, although in terms of the associated  $\Delta\Delta G$  value, the difference is not significant. Quite surprisingly however, the higher enantioselectivity for L-AChBP was also reflected in the biphasic curve obtained upon stop-flow recording of the binding rates ( $K_d/SF_{eq}$  values). The lower enantioselectivity (i.e., comparable affinities) of enantiomers (+)-4 R and (–)-4 S for A-AChBP ( $K_d$  values in the 2.2–5.4  $\mu M$  range) compared to L-AChBP (12–0.32  $\mu M$  range) justified the use of A-AChBP for the structural analyses.

#### 2.4. Overall View of the Crystalline Spiroimine-AChBP Complexes

The structures of A-AChBP bound with spiroimines (+)-4 R and (–)-4 S were solved in the 1.85–2.00 Å resolution range from preformed stoichiometric complexes (Table S1; Figure 4). Both showed the same tight homopentameric ring assembly of subunits as found in all previous AChBP structures (for reviews, see [69,70]). The ligand binding pocket encompasses a nest of five electron-rich aromatic side chains provided by residues Tyr93, Trp147, Tyr188 and Tyr195 on the principal (+) face of the subunit interface and residue Tyr55 on the complementary (–) face. This pocket is partially sheltered from the solvent by loop C, which is found at the outer perimeter of the pentamer and harbors at its tip a disulfide bridge linking the vicinal Cys190 and Cys191 residues, linked into a Cys-*trans*-Cys disulfide bridge (*aka* oxidized cysteinyl-cysteinyl ring), a signature determinant for nAChR  $\alpha$  subunits.

Both structures showed very similar positions of the bound spiroimines at all five subunit interfaces within a pentamer (see. r.m.s.d. values in *Experimental Procedures*). Despite the moderate binding affinities (Table 2), the well-defined electron densities revealed full ligand occupancy at all five binding sites (Figure 4) due to the high protein concentration (ca. 100-fold the  $K_d$  values) and slight molar excess of spiroimine over A-AChBP used for complex formation and crystallization (see *Experimental procedures*).

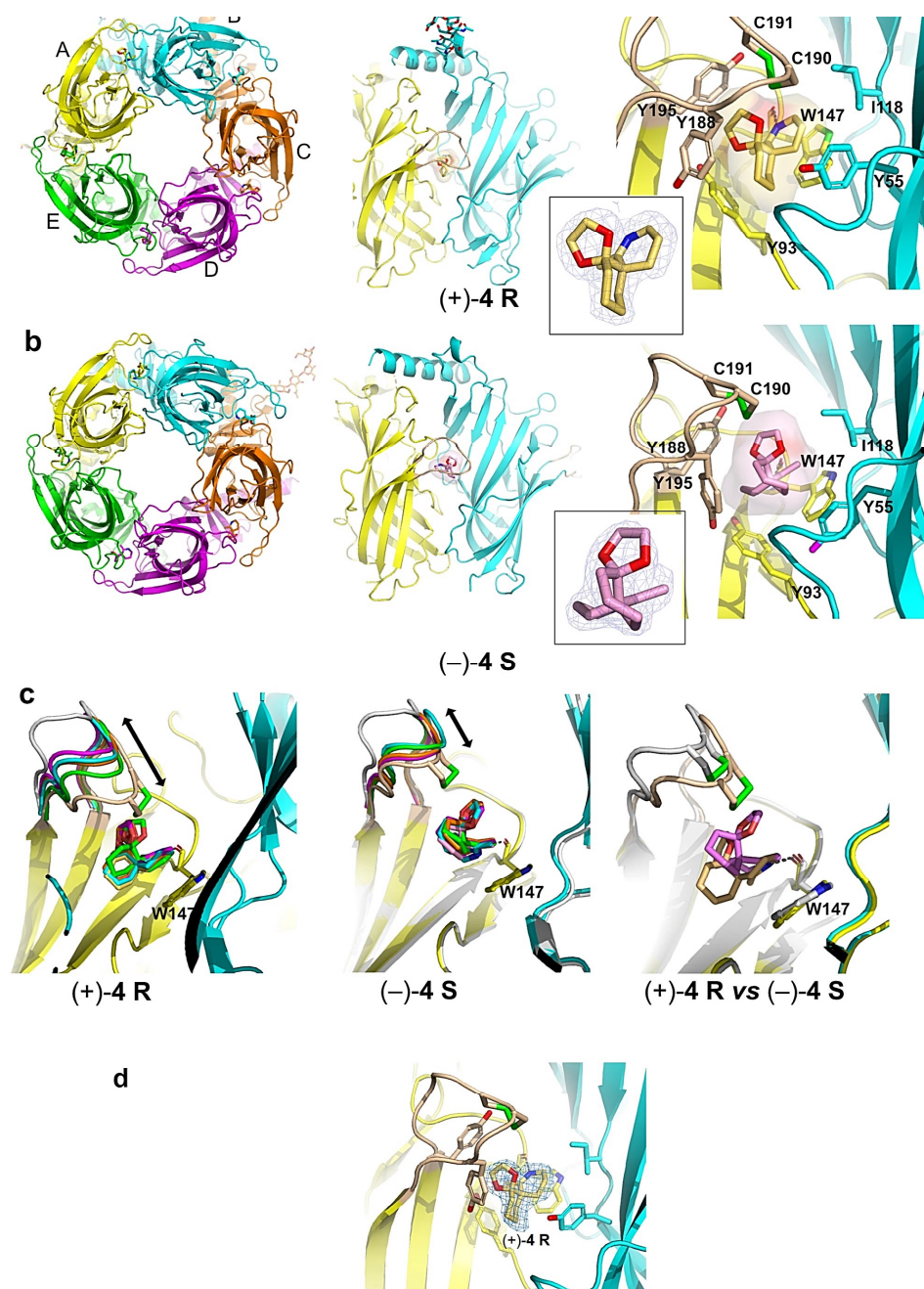


**Figure 4.** Overall and close-up views of the pentameric spiroimine-A-AChBP complexes. The A-AChBP pentamer in the (a) spiroimine (+)-4 R and (b) spiroimine (-)-4 S complexes is viewed from the “membrane” side (*left*), and in a radial perspective toward one subunit interface with the apical side at the top and the “membrane” side at the bottom (*center*). The clockwise labeling order of the subunits (A–E) denotes their contribution to the principal (+) and complementary (–) faces of each interface (A–B, B–C, etc.). Bound spiroimines (+)-4 R (light orange bonds and molecular surface, red oxygens, blue nitrogen) and (-)-4 S (pink bonds and molecular surface, red oxygens, blue nitrogen) are perfectly ordered, as assessed by the quality of the 1.8 Å- and 2.0 Å-resolution weighted 2Fo–Fc electron density maps contoured at 1.2σ (in blue) shown as insets. Close-up views (*right*) of the bound spiroimines in the aromatic nest at the subunit interface, showing details of their binding environment (radial perspective). The locations of the bound enantiomers are similar, but their main orientations differ. The side chains at the principal (+) and complementary (–) faces of the displayed interface that interact specifically with the spiroimines are displayed in yellow and cyan, respectively.

The Cys190-Cys191 disulfide bridge embedded at the tip of loop C is displayed in brown with green sulfur atoms. Dashed lines denote hydrogen bonds. The geometric parameters of key interactions between the spiroimine enantiomers and the side chains in the A-AChBP binding pocket are reported in Table S2. (c) Overlays of the five A-AChBP subunits in each of the (+)-4 **R** (left) and (–)-4 **S** (center) complex showing variations/fluctuations (arrow) in the loop C conformation, and of the (+)-4 **R** and (–)-4 **S** complexes (right). Loop C in apo A-AChBP is displayed in grey. (d) Close-up view of bound spiroimine (+)-4 **R** in the aromatic nest found at the subunit interface after A-AChBP co-crystallization with the (±)-4 racemate. The (+)-4 **R** identity of the bound enantiomer selected by A-AChBP from the racemate is evident. Color codes for the spiroimine enantiomers and A-AChBP loops and determinants are the same in all panels.

### 2.5. Detailed Description of the Crystalline Spiroimine-AChBP Complexes

In the A-AChBP complex with enantiomer (+)-4 **R**, the compact 3-ring skeleton of the spiroimine comfortably accommodates the core agonist signature motif central to the binding pocket (Figures 4 and 5) and ideally positions the 6-membered cyclic imine ring nearly parallel to the indole ring of Trp147 in loop B ( $\pi$ - $\pi$  stacking), and within H bond distances (2.6–2.7 Å) of the Trp147 carbonyl oxygen, with a typical  $\hat{H}$  angle value of  $\sim 125^\circ$  between the hydrogen bond donor, acceptor, and acceptor antecedent [78] (Table S2), as previously observed for the parental macrocyclic imine toxins (Figure 6). Such conservation of a *protonated* imine nitrogen (see discussion in [74] and reference 18 in it, along with the crystallization conditions in the *Experimental procedures*) tethers the spiroimine core centered within the binding pocket and greatly contributes to the binding affinity. The dioxolane ring makes nearly edge-to-face stacking interactions with Tyr188 and Tyr195 (loop C) from the (+) face, while the cyclohexane ring makes nearly face-to-face stacking interactions with Tyr93 from the (+) face and Tyr55 (loop D) from the (–) face (Figures 4 and A1). However, spiroimine binding involves virtually no interaction with residues from loop F at the complementary (–) face of the subunit interface (Figures 4, 5 and A1). This observation is consistent with the limited contribution of loop F to the binding of SPX and GYM *versus* its significant contribution for laterally accommodating the bridged ketal group specific to the pinnatoxins [71,72] (Figure 6).

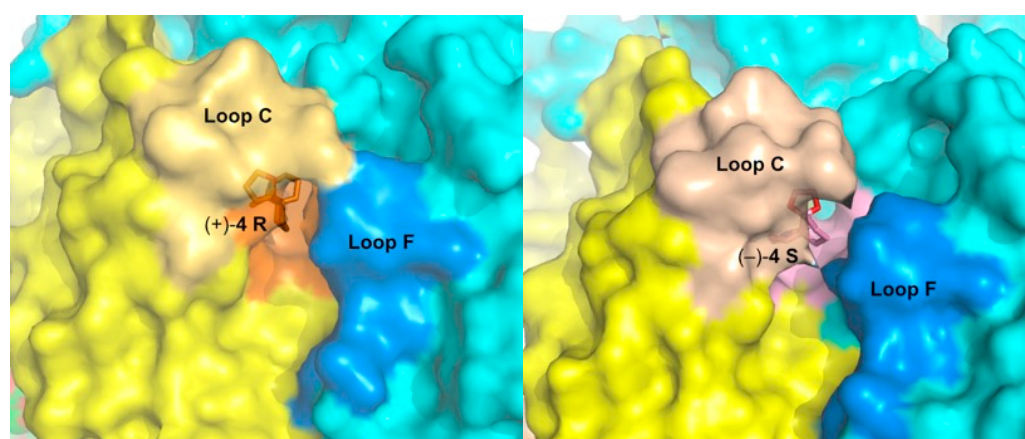


**Figure 5.** Molecular surfaces buried by the bound (+)-4 **R** (left, orange enantiomer and surface, gold capping loop C, blue loop F) and (–)-4 **S** (right, pink enantiomer and surface, beige capping loop C, blue loop F) at the A-AChBP subunit interface (yellow principal (+) face, cyan complementary (–) face), viewed radially from the pentamer outer periphery (same orientation as in Figure 4). The interfacial surface areas buried by the bound spiroimines of  $\sim 350 \text{ \AA}^2$  are two-fold smaller than those buried by the macrocyclic toxins ( $\sim 600\text{--}750 \text{ \AA}^2$  [71,72]).

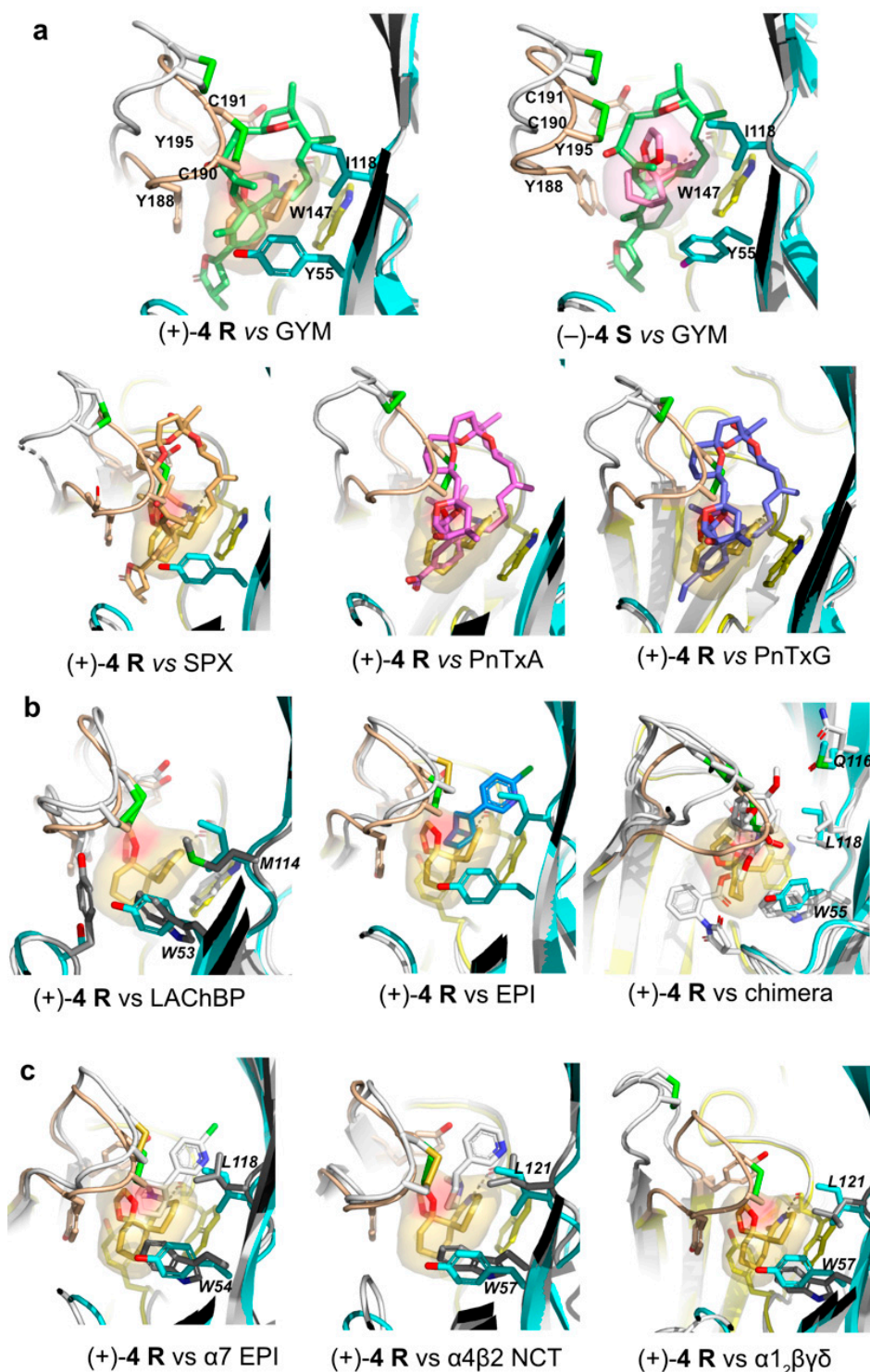


**Figure 6.** Structural comparison of the spiroimine-A-AChBP complexes with other AChBP and full-length nAChR complexes. Overlays of A-AChBP bound with enantiomers (+)-4 R and (-)-4 S with: A-AChBP bound with (a) the macrocyclic toxins GYM (green, PDB 2X00), SPX (orange, 2WZY), PnTxA (pink, 4XHE), PnTxG (purple, 4XK9); (b) L-AChBP in “apo” form (1I9B), A-AChBP bound with EPI (blue, 2BYQ), and A-AChBP- $\alpha 7$  chimera mutant II (white, 3SIO); (c) the *extracellular* LBDs of human  $\alpha 7$  nAChR bound to EPI (cryo-EM, 7KOQ), human  $\alpha 4\beta 2$  nAChR in the apo form (X-rays, 5KXI), and *Torpedo*  $\alpha 1_2\beta\gamma\delta$  nAChR in the apo form (cryo-EM, 7SMM). Residues in the ligand-binding pockets of L-AChBP and the three nAChRs that differ from those in A-AChBP are highlighted in grey and labeled in italics.

In the A-AChBP complex with enantiomer (−)-4 S, the cyclic imine ring, nearly perpendicular to the indole ring of Trp147 (T-shaped interaction), only partially overlaps that of the (+)-4 R enantiomer, with long-range H bond distances (2.8–3.5 Å) to the carbonyl oxygen of Trp147 and an  $\hat{H}$  angle value of  $\sim 142^\circ$  (Figures 4 and 5; Table S2). As a result, the position of the cyclohexane ring is displaced toward the tip of loop C, and the dioxolane ring projects in the opposite direction at the entrance of the binding pocket, thus making limited interactions with the A-AChBP residues. Such a drastic shift in the position of the 3-ring system for the two enantiomers is associated with differences in the loop-C position (Figures 4–6, and see below) and may account for the slightly (ca. 2-fold) higher affinity of enantiomer (+)-4 R for the two AChBPs compared to enantiomer (−)-4 S (Table 2). In turn, the one order of magnitude higher affinity of enantiomer (−)-4 S for L-AChBP compared to A-AChBP (Table 2; Figures 6b and A1) may correlate with the presence of substitutions Met114 (for Ile118) and Trp53 (for Tyr55) in the vicinity of the cyclic imine and cyclohexane rings. This is consistent with the ca. 5-fold higher affinity of enantiomer (+)-4 R compared with the (−)-4 S enantiomer for the  $\alpha 7$  and  $\alpha 4\beta 2$  nAChRs (Table 1; Figure A1). Here again, there is almost no interaction between the bound spiroimine and loop-F residues (Figures 4–5).

Co-crystallization of A-AChBP with the ( $\pm$ )-4 racemate unambiguously led to a bound (+)-4 R enantiomer at all five subunit interfaces in a virtually identical position to that seen in the (+)-4 R complex, with only a minor trace (i.e., occupancy below  $\sim 10\%$ ) of a bound (−)-4 S (Figure 4d). Per se, this observation would suggest a much lower dissociation rate for enantiomer (+)-4 R relative to its (−)-4 S congener than the one recorded through the binding studies (Table 2). Whether this is due to the more acidic and hydrophobic composition of the crystallization liquor used for the ( $\pm$ )-4 complex compared with the other two complexes (see Appendix D) or to conformational remodeling of the complex during crystal nucleation and growth [79] is unknown.

In all three complexes, the loop-C position shows a high degree of variability with respect to the different orientation of the 3-ring system in each enantiomer associated with slightly different orientations of the bound enantiomers at each binding interface (Figure 4c). In the (+)-4 R complex, loop C adopts a *closed*, agonist-bound position in one subunit along with a range of positions *intermediate* between those found in apo (2BYN) and agonist-bound A-AChBP (2BYQ, epibatidine) in the other four subunits. In the ( $\pm$ )-4 and (−)-4 S complexes, loop C clusters around *intermediate* positions in all five subunits. Moreover, at one interface of the (−)-4 S complex, the tip of loop C (Tyr188-Glu193) adopts two alternate conformations with up to 3 Å distance at position Cys190, an observation emphasizing the high conformational dynamics of loop C, even in the crystalline state. The average loop-C conformation in the spiroimine-AChBP complexes contrasts with the wide-open, “antagonist” position observed in the complexes with the parental, bulky macrocyclic spiroindoles/phyco toxins [71,72] or other large antagonists (Figure 6). However, the loop-C “intermediate” positions associated with its loose interactions with the spiroimines resemble more the position observed in HEPES-bound or apo AChBPs [63,67,80] than that in complexes with small agonists [65,67,68] (Figure 6). A reverse situation was reported for 2-aminopyrimidine agonists inducing an unusually large opening of loop C [81]. This comparative analysis further reflects the antagonist properties of these small spiroimines and illustrates, *here within a single AChBP pentamer*, how loop C can behave as a highly flexible sensor to adapt its configuration to the chemical features and position of the ligand within the binding pocket, as previously documented for many structurally-unrelated nicotinic ligands.

To explore a possible correlation between the spiroimine binding poses and interactions at the A-AChBP subunit interfaces and their binding affinities in each complex, from the structure coordinates, we calculated the DrugScore eXtended (DSX) scores, which combine distance-dependent atom–atom potentials, torsion angle potentials, and solvent-accessible surface-dependent potentials [82] (Table 3).

**Table 3.** DrugScore eXtended (DSX) scores for spiroimine binding at each A-AChBP subunit interface.

Interface	DSX Score (kJ/mol)		
	(+)-4 R Complex	(-)-4 S Complex	(±)-4 Complex
(A*-B)	-94.628 <sup>a</sup>	-77.480 <sup>b</sup>	-76.901 <sup>b</sup>
(B*-C)	-77.500 <sup>b</sup>	-69.469 <sup>b</sup>	-70.878 <sup>b</sup>
(C*-D)	-82.139 <sup>b</sup>	-67.328 <sup>b</sup>	-74.733 <sup>b</sup>
(D*-E)	-83.353 <sup>b</sup>	-64.331 <sup>b</sup>	-76.814 <sup>b</sup>
(E*-A)	-86.909 <sup>b</sup>	-68.729 <sup>b</sup>	-78.242 <sup>b</sup>
Mean score ± SD ( <i>n</i> = 5)	-84.906 ± 6.392	-69.467 ± 4.892	-75.514 ± 2.879

The subunit contributing the principal (+) face of each interface is indicated by an asterisk (see Figure 4). <sup>a</sup> Closed loop C. <sup>b</sup> Intermediate loop-C conformation. Smaller DSX score values reflect tighter binding. However, DSX scores do not represent the Gibbs free energy of interaction between the enantiomers and their binding surfaces and cannot be used to determine the respective K<sub>d</sub> values. Scores were calculated in Nanome (Nanome Inc., San Diego, CA, USA).

The smaller mean score for the interaction of enantiomer (+)-4 R at all five A-AChBP subunit interfaces compared to that for enantiomer (-)-4 S suggests tighter binding to A-AChBP, independently of the loop-C conformation. The ratio of the (+)-4 R/(-)-4 S mean scores, equal to 1.22, also indicates computational prediction from the structures for a tighter binding of enantiomer (+)-4 R, which should be reflected by a ca. one order of magnitude difference in the K<sub>d</sub> values for the two complexes [82]. The fact that our experimentally determined values do not differ that much from each other (Table 2) may arise either from differences in the “experimental” conditions or from five interfaces per complex making too small a statistical sample, or from the limited significance of comparing differences in affinities in the micromolar range, or, here again, from time-dependent conformational remodeling of the complexes in the crystal state but not during the binding experiments in solution [79]. Overall, the DX scoring approach appears consistent with the prevailing presence of enantiomer (+)-4 R in the structure of the complex prepared from the (±)-4 racemate (Figure 4).

## 2.6. Structural Comparisons

Certain features of the A-AChBP complexes with the (+)-4 R and (-)-4 S enantiomers closely resemble those found in the complexes with the bulkier macrocyclic imine compounds GYM and SPX (see r.m.s.d. values in *Experimental Procedures*), with in particular, the positions of the cyclic imine and cyclohexene rings (Figure 6). In fact, the orientation of the cyclic imine ring in the (-)-4 S complex virtually overlaps that of GYM. Structural overlay of these two complexes shows that the lack of the bis-spiroacetal/tetrahydrofuran and butyrolactone ring systems of GYM in the apical and membrane directions of the subunit interface, respectively, is partially compensated by the new dioxolane ring in the spiroimines that abuts against the Tyr188 and Tyr195 phenol rings in loop C. The loop-C conformational, large-amplitude motions observed across the five binding interfaces in the (+)-4 R and (-)-4 S complexes, coupled with alternate conformations of its tip (a behavior neither observed in complexes with macrocyclic phycotoxins nor in those with small agonists), appear to be a signature of the minimal spiroimine core motif. This comparison also suggests substituent modification at key positions around the 3-ring framework of spiroimines, notably in the cyclohexane ring, to confer greater binding selectivity and specificity on them. For example, a polar group attached to the cyclohexene ring would be expected to target residues in or near loop F at the complementary face of the subunit interface.

Comparisons with humanized A-AChBP- $\alpha$ 7-chimeras in the apo conformation [80] and the extracellular LBDs of the  $\alpha$ 4 $\beta$ 2,  $\alpha$ 7, and  $\alpha$ 1 $\beta$ 2 $\gamma$  $\delta$  nAChRs [59,60,83] showed a conserved aromatic nest with the exception of a Trp (in  $\alpha$ 4 and  $\alpha$ 7) or Arg ( $\alpha$ 1) residue in place of A-AChBP Tyr55 at the (-) face of the interface, and the positions of Tyr188 and Tyr195 within loop C at the (+) face (Figures 6 and A1; Table S2). Moreover, conservation of the “interacting” residues at the  $\alpha\gamma$  and  $\alpha\delta$  interfaces of the  $\alpha$ 1 $\beta$ 2 $\gamma$  $\delta$  nAChR is consistent



with the Hill slope of  $\sim 1$  observed in the functional assays (Figures 2, 6 and A1; Table S2). Concerning the  $\alpha 3\beta 2$  nAChR, which was not included in the present study, a similar binding mode and antagonistic potency as for the  $\alpha 4\beta 2$  subtype can be predicted due to their high sequence homology in the spiroimine binding site (see Figure S1 in [70]).

### 3. Experimental Procedures

#### 3.1. Chemical Synthesis, Separation, and Enantiomeric Characterization of the Spiroimines

Racemic spiroimine was synthesized from diketone **1** by alkylation with 1-azido-3-iodopropane in the presence of anhydrous cesium carbonate to afford the azido- $\beta$ -keto ketone ( $\pm$ )-**2** in 53% yield (Scheme 1; Appendix B). The cyclohexanone function of ( $\pm$ )-**2** was then protected with ethylene glycol to generate the corresponding dioxolane ( $\pm$ )-**3** in 31% yield. Then, the azide function of ( $\pm$ )-**3** was reduced with triphenylphosphine, followed by cyclization under basic conditions to generate spiroimine ( $\pm$ )-**4** in 83% yield. Each compound was characterized by  $^1\text{H}$  and  $^{13}\text{C}$  NMR spectroscopy in  $\text{CDCl}_3$  (Figures S1–S6). The two enantiomers present in a 1:1 ratio in ( $\pm$ )-**4** were then separated by semi-preparative chiral HPLC in Hept/EtOH 80:20 (*v/v*) to afford (+)-**4** ( $t = 4.54$  min,  $\alpha_{\text{D}}^{24} = +144.5$ ) ( $c = 0.25$ ,  $\text{CHCl}_3$ ) and (–)-**4** ( $t = 6.21$  min,  $\alpha_{\text{D}}^{24} = -163.5$ ) ( $c = 0.25$ ,  $\text{CHCl}_3$ ) with a purity greater than 99% (Figure S7). The racemate and pure enantiomers were lyophilized and stored at  $-20$  °C. Stock solutions at 10 mM (racemate) and 20 mM (enantiomers) in MeOH prepared from the lyophilized compounds were stored as aliquots at  $-80$  °C.

The synthesis of enantiomer (–)-**4** from ketone **5** (a mixture of (+)-**5 S** and (–)-**5 R** in a 90:10 molar ratio, prepared according to [76]), was adapted from [74]. In brief, Ru-catalyzed cross-metathesis with vinyl pinacol boronate (step 1), followed by oxidation, then reduction (step 2), afforded the primary alcohol (not shown). The latter was converted into the azide (step 3), which was reduced with triphenylphosphine (step 4) to give spiroimine (–)-**4** ( $\alpha_{\text{D}}^{24} = -47.3$ ) ( $c = 0.25$ ,  $\text{CHCl}_3$ ) (Scheme 2), of absolute configuration (S) at the quaternary carbon, as indicated by the negative sign of the optical rotation.

#### 3.2. Analysis of ACh-Evoked Currents

The sources for live animals and biological materials, the procedures for nAChR microtransplantation and expression in oocytes, and the procedures for manual ( $\alpha 1_2\beta\gamma\delta$  nAChR) and automated ( $\alpha 7$  and  $\alpha 4\beta 2$  nAChRs) TEVC recording are detailed in Appendix C. In brief, our TEVC protocol comprised 2 to 3 pulses of ACh at a concentration equivalent to its  $\text{EC}_{50}$  value, such as: 15 s at 25  $\mu\text{M}$  for  $\alpha 1_2\beta\gamma\delta$  nAChR, 5 s at 100  $\mu\text{M}$  for  $\alpha 7$  nAChR, 15 or 30 s at 150  $\mu\text{M}$  for  $\alpha 4\beta 2$  nAChR (perfusion flow, 8 mL/min). Then, the oocyte was perfused for 45 s with the tested spiroimine at a given concentration, immediately followed by the co-application of ACh and the spiroimine at the same concentrations and times as indicated above. The oocyte was washed with Ringer's solution, and then recovery of the ACh-evoked current was recorded.

The concentration–inhibition curves were analyzed as previously detailed [71,72] using the equation  $I = I_{\text{max}} [L]^{n\text{H}} / (\text{EC}_{50}^{n\text{H}} + [L]^{n\text{H}})$  (Equation (1)), where  $I$  is the measured agonist-evoked current,  $[L]$  is the agonist concentration,  $\text{EC}_{50}$  is the agonist concentration that evoked half the maximal current ( $I^{\text{max}}$ ), and  $n\text{H}$  is the Hill coefficient. For antagonist inhibition, current ( $I$ ) values were normalized to the  $I^{\text{max}}$  value recorded from the same oocyte to yield the fractional (%) response data.  $\text{IC}_{50}$  values were established from the concentration–response curves by fitting to the equation  $F = 1 / [1 + ([X] / \text{IC}_{50})^{n\text{H}}]$  (Equation (2)), where  $F$  is the fractional response obtained in the presence of the inhibitor at concentration  $[X]$ , and  $\text{IC}_{50}$  is the inhibitor concentration reducing the ACh-evoked amplitude by half. Data analysis was performed without constraints as  $\text{Log}[\text{spiroimine}]$  versus response (three parameters), with a Hill slope  $\sim 1$ . Statistical significance of differences between the control and test values was assessed using either the two-tailed Student's " $t$ " test or the Kolmogorov–Smirnov two-sample test and  $p < 0.05$ .

### 3.3. Ligand Binding to the AChBPs

The procedures for stable expression and purification of A- and L-AChBPs are described in Appendix D. Rate constants for association ( $k_{\text{on}}$ ) and dissociation ( $k_{\text{off}}$ ) were determined by multiple kinetic means, largely as previously described [64,67,71,72]. Measurement of  $k_{\text{on}}$  and  $k_{\text{off}}$  values entailed the direct admixture of reactants and monitoring the quenching of AChBP native Trp fluorescence. Individual rate constants were determined from linear regression of the experimental mono-exponential decay of Trp fluorescence intensity ( $k_{\text{obs}}$ ) using the linear “approach-to-equilibrium” relationship  $k_{\text{obs}} = k_{\text{on}}[\text{spiroimine}] + k_{\text{off}}$  (Equation (3)). Additional measurements of  $k_{\text{off}}$  ( $k_{\text{off}/\text{GAL}}$ ) employed stopped-flow measurement of the rate of occupation of free AChBP binding sites by a competing ligand (gallamine, used in large excess relative to its  $K_{\text{d}}$ ) to form a non-quenching gallamine-AChBP complex. Equilibrium dissociation constants were determined either from the ratios of rate constants ( $K_{\text{d}}/(k_{\text{off}}/k_{\text{on}})$ ), or from stopped-flow measurements of the rates of gallamine or epibatidine binding to pre-equilibrated spiroimine-AChBP complexes formed using increasing spiroimine concentrations ( $K_{\text{d}/\text{SFeq}}$ ), or by the scintillation proximity assay (SPA) where spiroimine competition against the binding of [ $^3\text{H}$ ]epibatidine (to L-AChBP) or [ $^3\text{H}$ ]methyllycaconitine (to A-AChBP) was monitored at equilibrium ( $K_{\text{d}/\text{SPAeq}}$ ). In brief, in the SPA assay, to titrate those binding sites made available upon toxin dissociation, each equilibrated spiroimine-AChBP complex, at 250 pM in binding sites and a slight molar excess of toxin, was mixed with the [ $^3\text{H}$ ]ligand at a concentration well above its  $K_{\text{d}}$  value. The time course of [ $^3\text{H}$ ]ligand binding was monitored over several hours. All experiments were performed in triplicate, in which individual data differed by less than 20%.

### 3.4. Structure Determination and Refinement

The procedures for the formation and crystallization of the spiroimine-A-AChBP complexes and for data collection are described in Appendix D. The structure of the A-AChBP complex with spiroimine (+)-4 **R** was solved by molecular replacement with PHASER [84] using the apo A-AChBP structure (PDB: 2BYN [67]) as a search model, and that of the complex with spiroimine (−)-4 **S** by difference Fourier synthesis with REFMAC [85]. The models of the spiroimine-A-AChBP complexes were improved by manual adjustment with COOT [86] and refined with REFMAC including TLS refinement with each subunit defining a TLS group. In each case, a random set of reflections was set aside for cross-validation purposes. The molecular structures of spiroimines (+)-4 **R** and (−)-4 **S** and the associated library files containing the stereochemical and parametric data were generated with SKETCHER [87]. Ligands were fitted into unbiased Fo–Fc difference electron density maps calculated after 10 cycles of rigid-body refinement. Automated solvent building used COOT. The A-AChBP-spiroimine interfaces were analyzed with the PISA server [88]. Data collection and refinement statistics are reported in Table S1.

The final structures comprise A-AChBP residues His1–Arg207/Arg208 for each subunit in the single homopentamer present in the asymmetric unit, and a fully resolved spiroimine in each of the five binding sites. For each complex, the N-terminal FLAG sequence could be fully resolved in one of the five subunits, and a tetrasaccharide moiety linked to Asn74 was visible in another subunit. High temperature factors and weak electron densities were associated with the other four FLAG sequences and with the five surface loops Asn15–Met19. Five chlorine ions in the (+)-4 **R** complex and one isopropanol molecule and six chlorine ions in the (−)-4 **S** complex (all arising from the crystallization liquor or the purification buffer) could also be modeled. Quality of the models was validated using COOT and MOLPROBITY [89], with ~97% of residues in favored regions of the Ramachandran plot and no outliers. Data collection and refinement statistics are reported in Table S1.

### 3.5. Structural Analyses and Comparisons

Comparison of the spiroimine-A-AChBP complexes with other AChBP structures included those of A-AChBP in the apo form (PDB: 2BYN [67]) and bound with phycotoxins SPX and GYM (2WZY and 2X00 [71]), pinnatoxins PnTxA and PnTxG (4XHE and 4XK9 [72]), and the small agonist representative, EPI (2BYQ [67]); of L-AChBP in the “apo” (HEPES-bound) form (119B [63]); and of humanized A-AChBP- $\alpha 7$ -chimeras (mutants I and II; 3T4M and 3SIO [80]). The average root-mean-square deviation (r.m.s.d) between A-AChBP subunits bound with spiroimine (+)-**4 R** with *closed* and *intermediate* states of loop C is 0.6 Å; between the five A-AChBP subunits bound with spiroimine (–)-**4 S** with *intermediate* states of loop C, it is 0.27 Å; between the A-AChBP subunits bound to spiroimine (+)-**4 R** with a *closed* loop C versus bound to spiroimine (–)-**4 S** with an *intermediate* state of loop C, it is 0.43 Å; and between the nine A-AChBP subunits with *intermediate* states of loop C, it is in the 0.27–0.43 Å range (all for 204–210 C $\alpha$  atoms).

Comparisons with structures of full-length nAChRs included the human  $\alpha 7$  bound to EPI (cryo-EM structure 7KOQ [59]), the human  $\alpha 4\beta 2$  in the apo form (X-ray structure 5KXI [60]), and the *Torpedo*  $\alpha 1_2\beta\gamma\delta$  receptor in the apo form (cryo-EM structure 7SMM [83]). The average r.m.s.d. between A-AChBP subunits bound with spiroimine (+)-**4 R** with a *closed* loop C or with spiroimine (–)-**4 S** with an *intermediate* loop C and the extracellular ligand-binding domains of the above-mentioned nAChRs is in the 1.3–1.7 Å range for 181–194 C $\alpha$  atoms.

### 3.6. Figures

Figure 1 was generated with Marvin (ChemAxon); Schemes 1 and 2 and those in Appendix B with ChemDraw; Figures 2 and 3 with GraphPad Prism 9.0 (GraphPad Software, San Diego, CA, USA) and pCLAMP 9.0 (Molecular Devices, LLC., San Jose, CA, USA); Figures 4–6 with PyMOL [90]; Figure A1 with ESPript [91]; Figures S1–S6 with TopSpin; and Figure S7 with MassLynx.

## 4. Concluding Remarks

These data emphasize the intrinsic capacity of the spiroimine enantiomers synthesized in this study to block selected nAChR subtypes in a competitive manner, highlight the major contribution of the spiroimine core of macrocyclic imine toxins to binding within the nAChR aromatic nest (*aka* “agonist-competitive antagonist site” [92]), and confirm the need for extended interaction networks as established by the macrocyclic toxins to define high affinities and the variable levels of subtype specificity dictated by their capacity to extend in all directions of the subunit interface. Hence, this study identifies a minimal set of functional pharmacophores and binding determinants (Table S2) as templates for designing second-generation spiroimine-like bioactive molecules with full antagonistic properties targeting disease-associated nAChR subtypes. From that perspective, enantiomer (+)-**4 R**, with its higher specificity for the  $\alpha 1_2\beta\gamma\delta$  nAChR compared with the  $\alpha 7$  and  $\alpha 4\beta 2$  subtypes, and its tighter binding to key residue Trp147 in the A-AChBP binding pocket compared with enantiomer (–)-**4 S**, appears as a suitable starting point in a context of muscle-linked diseases.

These data also contribute to challenge a conclusion built over the years that small molecules containing a quaternary nitrogen and strictly occupying the agonist binding pocket at the subunit interface, without extending substituents outside of this core, cannot act as nicotinic antagonists. Initial insights against this “dogma” include the small cyclic, disulfide-containing marine molecule, nereistoxin (*aka* *N,N*-dimethyl-1,2-dithiolan-4-amine), shown to act as a nicotinic antagonist with sub-millimolar IC<sub>50</sub> values [93]. Availability of a crystal structure of a nereistoxin-AChBP complex would be of interest to complement the current study.

**Supplementary Materials:** The following supporting information can be downloaded from <https://www.mdpi.com/article/10.3390/md22040149/s1>. Figure S1:  $^1\text{H}$  NMR spectrum ( $\text{CDCl}_3$ ) of 2-acetyl-2-(3-azidopropyl)cyclohexanone ( $\pm$ )-2. Figure S2:  $^{13}\text{C}$  NMR spectrum ( $\text{CDCl}_3$ ) of 2-acetyl-2-(3-azidopropyl)cyclohexanone ( $\pm$ )-2. Figure S3:  $^1\text{H}$  NMR spectrum ( $\text{CDCl}_3$ ) of 1-[6-(3-azidopropyl)-1,4-dioxaspiro[4.5]dec-6-yl]ethanone ( $\pm$ )-3. Figure S4:  $^{13}\text{C}$  NMR spectrum ( $\text{CDCl}_3$ ) of 1-[6-(3-azidopropyl)-1,4-dioxaspirodec-6-yl]ethanone ( $\pm$ )-3. Figure S5:  $^1\text{H}$  NMR spectrum ( $\text{CDCl}_3$ ) of 7-methyl-1,4-dioxo-8-azadispiropentadec-7-ene ( $\pm$ )-4. Figure S6:  $^{13}\text{C}$  NMR spectrum ( $\text{CDCl}_3$ ) of 7-methyl-1,4-dioxo-8-azadispiropentadec-7-ene ( $\pm$ )-4. Figure S7: Separation of enantiomers (+)-4 and (−)-4 from the ( $\pm$ )-4 racemate by chiral HPLC. Table S1: X-ray crystallography—Data collection and refinement statistics. Table S2: Geometric parameters of key interactions between the (+)-4 **R** and (−)-4 **S** enantiomers and side chains in the A-AChBP binding pocket.

**Author Contributions:** Conceptualization, R.A., Z.R., C.G., J.M. and P.M.; Methodology, Y.B., G.S., L.C., R.A., Z.R., C.G., J.M. and P.M.; Validation, Y.B., G.S., L.C., R.A., Z.R., P.T., C.G., J.M. and P.M.; Formal analysis, Y.B., G.S., L.C., R.A., Z.R., S.C., C.G., J.M. and P.M.; Investigation, Y.B., G.S., L.C., R.A., Z.R. and S.C.; Resources, Y.B., G.S., R.A., Z.R., P.T., C.G., J.M. and P.M.; Data curation, Y.B., G.S., R.A., Z.R. and P.M.; writing—original draft preparation, Y.B., G.S., L.C., R.A., Z.R., C.G., J.M. and P.M.; Writing—review and editing, Y.B., G.S., L.C., R.A., Z.R., C.G., J.M. and P.M.; Visualization, Y.B., G.S., L.C., R.A., Z.R., J.M. and P.M.; Supervision, P.T., C.G., J.M. and P.M.; Project administration, C.G., J.M. and P.M.; Funding acquisition, Y.B., L.C., R.A., P.T., C.G., J.M. and P.M. All authors have read and agreed to the published version of the manuscript.

**Funding:** This work was supported by an ICSN-CNRS grant (to C.G. and L.C.); grants NEUROSPIROIMINE ANR-PCV-07-194417 (to J.M.), ICH-NEURO-MET ANR-21-CE34-0024 (to R.A.), and FRISBI ANR-10-INSB-0005 (to the AFMB laboratory); USPHS grants R37-GM18360 and P42-ES-010337 (to P.T.); and the CNRS/AMU/UCSD Associated International Laboratory “Structure-Guided Investigations into Disease States and Therapeutic Strategies” (LIA SGIDSTS) (to P.M. and P.T.).

**Institutional Review Board Statement:** The *Torpedo marmorata* fish and *Xenopus laevis* frogs used for this study were maintained and treated in strict adherence with the European Community guidelines for laboratory animal handling, and according to a protocol approved by the Ethical Committee for Animal Experimentation (C2EA-59 of Paris Center-South, to R.A.). All efforts were made to minimize animal suffering and to reduce the number of animals used. All animal experimental procedures were approved by the Animal Ethics Committee of the CEA, by the French General Directorate for Research and Innovation (project APAFIS#5310-2016042016067330 v3 protocol authorized to R.A.).

**Data Availability Statement:** The data presented in this study are included in the main text, Appendix A, and the Supplementary Materials. The atomic coordinates and structure factors of the A-AChBP complexes with enantiopure spiroimines (+)-4 **R** and (−)-4 **S** and the ( $\pm$ )-4 racemate have been deposited at the RCSB-PDB ([www.rcsb.org](http://www.rcsb.org)) with accession codes 8Q1M, 8QTL, and 8QX2, respectively.

**Acknowledgments:** We gratefully acknowledge the expert assistance of Kwok-Yiu Ho (UCSD, La Jolla, CA) for the AChBP binding assays and Karine Barral, Philippe Leone, Julien Lescar, Miguel Ortiz-Lombardia, Florence Vincent (AFMB lab), Sébastien Santini (IGS, Marseille), the ID14-EH1 and ID23-1 staff of the European Synchrotron Radiation Facility (ESRF, Grenoble), and the Proxima-1 staff of the SOLEIL synchrotron (Gif-sur-Yvette) during data collection. We thank Isabel Bermudez (Oxford Brookes University, Oxford, UK) and Pierre-Jean Corringer (Institut Pasteur, Paris, France) for the kind gift of the nAChR subunit cDNAs.

**Conflicts of Interest:** The authors declare no conflicts of interest. The funders had no role in the design of the study; in the collection, analysis, or interpretation of data; in the writing of the manuscript; nor in the decision to publish the results.

## Appendix A.

### *Receptors Used or Mentioned in this Study*

The prototype of vertebrate skeletal muscle nAChR, found in large amounts in the *Torpedo* electric organ, is a transmembrane heteropentameric assembly of four homologous subunits with a  $\alpha_1\alpha_2\beta\gamma\delta$  stoichiometry (Figure A1). Nicotinic agonists and competitive antagonists bind with distinctive affinities at the two,  $\alpha/\gamma$ , and  $\alpha/\delta$  subunit interfaces.

In the peripheral and central nervous systems, the human  $\alpha 4\beta 2$  subtype, which plays predominant roles in both pre- and postsynaptic functions, has variable stoichiometries involving two or three  $\alpha/\beta$  subunit interfaces and ligand binding sites. Typically, agonist binding to the two or three sites of the  $\alpha 1_2\beta\gamma\delta$  or  $\alpha 4\beta 2$  nAChR in the closed channel state selects conformational transitions leading to channel opening, and then to nAChR desensitization. Competitive antagonist binding to at least one site blocks channel function. When the affinities of the two sites differ, the antagonism of function correlates with the occupation of the higher affinity site [94]. In turn, the homopentameric  $\alpha 7$  subtype, also found at pre- and postsynaptic neuronal locations, encompasses five interfacial  $\alpha/\alpha$  binding sites with identical affinity [95].

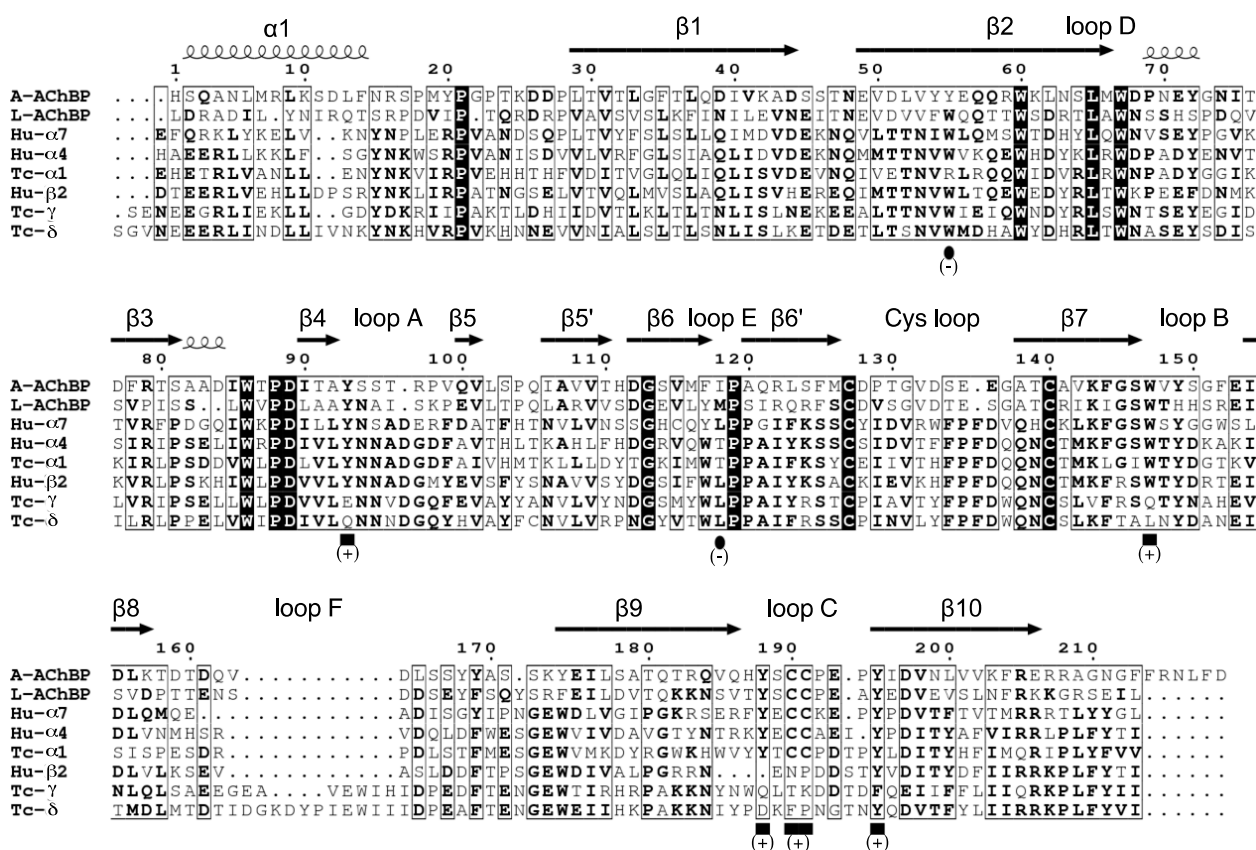


**Figure A1.** Sequence alignment for the extracellular ligand-binding domains of the AChBP and nAChR subunits related to this study. The A-AChBP secondary structure elements, along with loops A (or  $\beta 4$ - $\beta 5$ ), B ( $\beta 7$ - $\beta 8$ ), C ( $\beta 9$ - $\beta 10$ ), D ( $\beta 2$ ), E ( $\beta 6$ - $\beta 6'$ ), F ( $\beta 8$ - $\beta 9$ ), and the Cys-loop ( $\beta 6'$ - $\beta 7$ ), are indicated and labeled above the alignment. Below the alignment, A-AChBP residues, whose side chains interact with the bound spiroimines and are conserved in L-AChBP and nAChR subunits  $\alpha 1$ ,  $\alpha 4$ ,  $\alpha 7$ , are indicated by squares, while interacting non-conserved residues are indicated by ovals. Assignment of these residues to the principal (+) and complementary (-) faces of the subunit interface is indicated by the corresponding signs.

## Appendix B.

### Appendix B.1. Chemical Synthesis of 2-acetyl-2-(3-azidopropyl)cyclohexanone ( $\pm$ )-2 ( $C_{11}H_{17}N_3O_2$ , 223.2760) (Figure A2)

To a solution of diketone **1** (0.49 mL, 3.79 mmol) in dry DMF (6 mL) was added anhydrous cesium carbonate (102.3 mg, 4.17 mmol) at RT. The mixture was stirred for 10 min, then 1-azido-3-iodopropane (1.6 g, 7.58 mmol) was added and the mixture stirred for 20 h at RT. The reaction was quenched with a saturated NaCl solution and the aqueous layer extracted with ethyl acetate. The combined organic layers were washed with a

saturated NaCl solution and dried over  $\text{MgSO}_4$ . The solvent was evaporated under vacuum and the residue purified over silica gel (Hept to Hept/EtOAc: 8/2) to afford a colorless oil (446 mg, 53%).

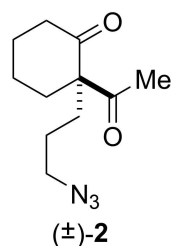


**Figure A2.** Chemical structure of the 2-acetyl-2-(3-azidopropyl)cyclohexanone racemate.

IR:  $\nu$  (film) 2941–2867, 2090, 1713, 1693  $\text{cm}^{-1}$ . MS: (ESI)  $m/z$ : 246 (100) [M + Na]. HRMS: calculated for  $\text{C}_{11}\text{H}_{17}\text{O}_2\text{Na}$ : 246.1218; found: 246.1211.  $^1\text{H}$ : (300 MHz;  $\text{CDCl}_3$ )  $\delta$  3.28 (t,  $J = 6.5$  Hz, 2H), 2.46 (m, 2H), 2.29 (m, 1H), 2.10 (s, 3H), 2.04–1.84 (m, 2H), 1.80–1.59 (m, 4H), 1.52–1.30 (m, 3H).  $^{13}\text{C}$ : (75 MHz;  $\text{CDCl}_3$ )  $\delta$  209.8 (Cq), 206.6 (Cq), 67.2 (Cq), 51.5 ( $\text{CH}_2$ ), 41.6 ( $\text{CH}_2$ ), 34.3 ( $\text{CH}_2$ ), 31.1 ( $\text{CH}_2$ ), 27.1 ( $\text{CH}_2$ ), 26.1 ( $\text{CH}_3$ ), 23.6 ( $\text{CH}_2$ ), 22.1 ( $\text{CH}_2$ ).

*Appendix B.2. Chemical Synthesis of 1-[6-(3-azidopropyl)-1,4-dioxaspiro[4.5]dec-6-yl]ethanone (±)-3 ( $\text{C}_{13}\text{H}_{21}\text{N}_3\text{O}_3$ , 267.3290) (Figure A3)*

To a solution of diketone (±)-**2** (180 mg, 0.807 mmol) in toluene (2 mL) was added ethylene glycol (0.09 mL, 1.61 mmol). A catalytic amount of para-toluene sulfonic acid was then introduced. The flask was fitted with a Dean–Stark and the solvent heated under reflux overnight. The reaction was quenched with a saturated  $\text{Na}_2\text{CO}_3$  solution and the aqueous phase extracted twice with ethyl acetate. The combined organic layers were washed with brine dried over  $\text{Na}_2\text{SO}_4$ . The solvent was evaporated under vacuum and the crude was purified over silica gel (Hept to Hept/EtOAc: 8/2) to afford a colorless oil ( $m = 66.1$  mg, 31%).

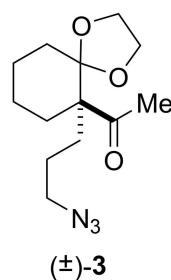


**Figure A3.** Chemical structure of the 1-[6-(3-azidopropyl)-1,4-dioxaspiro[4.5]dec-6-yl]ethanone racemate.

IR:  $\nu$  (film) 2936–2866, 2091, 1697, 1177  $\text{cm}^{-1}$ . MS: (ESI)  $m/z$ : 290 (100) [M + Na]. HRMS: calculated for  $\text{C}_{13}\text{H}_{21}\text{N}_3\text{O}_3\text{Na}$ : 290.1481; found: 290.1483.  $^1\text{H}$ : (500 MHz;  $\text{CDCl}_3$ )  $\delta$  3.98–3.85 (m, 4H), 3.26 (dd,  $J = 6.7, 6.7$  Hz, 2H), 2.22 (s, 3H), 2.06 (m, 2H), 1.69 (m, 1H), 1.64–1.56 (m, 3H), 1.54–1.40 (m, 4H), 1.35 (m, 1H), 1.16 (m, 1H).  $^{13}\text{C}$ : (75 MHz;  $\text{CDCl}_3$ )  $\delta$  210.9 (Cq), 111.1 (Cq), 64.4 ( $\text{CH}_2$ ), 64.0 ( $\text{CH}_2$ ), 58.4 (Cq), 51.8 ( $\text{CH}_2$ ), 31.6 ( $\text{CH}_2$ ), 28.9 ( $\text{CH}_3$ ), 28.8 ( $\text{CH}_2$ ), 27.6 ( $\text{CH}_2$ ), 23.5 ( $\text{CH}_2$ ), 22.9 ( $\text{CH}_2$ ), 20.7 ( $\text{CH}_2$ ).

*Appendix B.3. Chemical Synthesis of 7-methyl-1,4-dioxo-8-azadispiro[4.0.5.4]pentadec-7-ene (±)-4 ( $\text{C}_{13}\text{H}_{21}\text{NO}_2$ , 223.3160) (Figure A4)*

To a solution of azide (±)-**3** (22.3 mg, 83  $\mu\text{mol}$ ) in THF:H<sub>2</sub>O (9:1, 1.2 mL) was added trimethylphosphine (1 M in toluene, 87  $\mu\text{L}$ , 87  $\mu\text{mol}$ ) under argon. The mixture was stirred overnight at RT. The solvent was evaporated under vacuum and the crude mixture dissolved in methanol (3 mL), then ammonia (28%, 1 mL) was added. The mixture was heated to 80  $^\circ\text{C}$  for 2 h. The solvent was evaporated and the residue purified over silica

gel (DCM with 1% NH<sub>4</sub>OH to DCM/MeOH/95/5 with 1% NH<sub>4</sub>OH) to give a colorless oil (m = 15.4 mg, 83%).

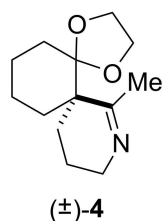


**Figure A4.** Chemical structure of the 7-methyl-1,4-dioxo-8-azadispiro[4.0.5.4]pentadec-7-ene racemate.

IR:  $\nu$  (film) 3364, 2927–2865, 1638, 1089 cm<sup>-1</sup>. MS: (ESI)  $m/z$ : 224 (100) [M + H]. HRMS: calculated for C<sub>13</sub>H<sub>22</sub>NO<sub>2</sub>: 224.1651; found: 224.1659. <sup>1</sup>H: (500 MHz; CDCl<sub>3</sub>)  $\delta$  3.90–3.77 (m, 4H), 3.56 (m, 2H), 3.48 (m, 2H), 2.20 (ddd,  $J$  = 13.1, 5.2, 4.8 Hz, 1H), 2.15 (s, 3H), 2.07 (m, 1H), 1.92 (m, 1H), 1.71 (ddd,  $J$  = 13.1, 4.8, 4.8 Hz, 1H), 1.66–1.57 (m, 2H), 1.56–1.33 (m, 6H). <sup>13</sup>C: (75 MHz; CDCl<sub>3</sub>)  $\delta$  172.8 (Cq), 113.2 (Cq), 64.6 (CH<sub>2</sub>), 63.8 (CH<sub>2</sub>), 48.8 (CH<sub>2</sub>), 46.1 (Cq), 33.9 (CH<sub>2</sub>), 31.3 (CH<sub>2</sub>), 28.5 (CH<sub>2</sub>), 26.5 (CH<sub>3</sub>), 23.1 (CH<sub>2</sub>), 19.7 (CH<sub>2</sub>), 19.6 (CH<sub>2</sub>).

## Appendix C.

### Appendix C.1. Live Animals and Biological Materials

*Torpedo marmorata* fish and adult female *Xenopus laevis* frogs were purchased live from the Station Biologique de Roscoff (CNRS-Sorbonne Université, Roscoff, France) and the TEFOR Paris-Saclay (Gif sur Yvette, France). The cDNAs encoding the subunits forming the human  $\alpha 7$  neuronal nAChR and  $\alpha 4\beta 2$  subtypes were kindly provided by Isabel Bermudez (Oxford Brookes University, Oxford, UK) and Pierre-Jean Corringer (Institut Pasteur, Paris, France), respectively.

### Appendix C.2. Microtransplantation and Expression of the nAChRs in *Xenopus* Oocytes

Stage V–VI *Xenopus laevis* oocytes [96] were surgically removed from mature female frogs by laparotomy under tricaine (ethyl 3-aminobenzoate methanesulfonate salt, Sigma Aldrich, Saint Quentin, France) anesthesia, and placed in a Ca<sup>2+</sup>-free medium made of HEPES 5 mM pH 7.6, NaCl 88 mM, KCl 2.5 mM, and MgCl<sub>2</sub> 1 mM [97]. Oocytes were defolliculated manually and maintained at 18 °C in a Barth's solution made of HEPES 7.5 mM pH 7.6, NaCl 88 mM, KCl 1 mM, CaCl<sub>2</sub> 0.41 mM, MgSO<sub>4</sub> 0.82 mM, Ca(NO<sub>3</sub>)<sub>2</sub> 0.33 mM, NaHCO<sub>3</sub> 2.5 mM, and supplemented with kanamycin 0.1 mg/mL [98–100].

*Torpedo* membranes containing  $\alpha 1_2\beta\gamma\delta$  nAChR were microtransplanted into the oocyte cytoplasm by microinjecting a membrane suspension (50 nL at 2.5  $\mu\text{g}/\mu\text{L}$ , i.e., 125 ng total protein, in 5 mM glycine) [101] with an electronic micro-injector (Nanoliter2000 Micro4 Controller, World Precision Instruments Inc., Hertfordshire, UK) mounted on a microscope [99]. Human  $\alpha 7$  and  $\alpha 4\beta 2$  nAChRs were expressed through microinjection, into the oocyte nucleus, of  $\alpha 7$  mRNA and of a 1:1 ( $w/w$ ) mixture of  $\alpha 4$  and  $\beta 2$  cDNAs (a ratio favoring expression of the  $\alpha 4_3\beta 2_2$  population over the  $\alpha 4_2\beta 2_3$  population) (50 nL at 1  $\mu\text{g}/\mu\text{L}$ ) in a pRc/CMV expression vector (Invitrogen) [102]. Oocytes were maintained at 18 °C and TEVC recordings were performed 1–4 days later in a room with controlled temperature (20 °C).

### Appendix C.3. Voltage-Clamp Recordings in Oocytes

Manual TEVC on  $\alpha 1_2\beta\gamma\delta$  nAChR oocytes was carried out using an OC-725B amplifier (Warner Instrument Corp., Hamden, CT, USA). Voltage and current borosilicate glass micro-electrodes were filled with KCl 3 M and had 0.5–1.5 M $\Omega$  tip resistances. For data acquisition and recording, a pCLAMP-9/Digidata-1322A system (Molecular Devices, San Jose, CA, USA) was used. The oocyte recording chamber of 300  $\mu\text{L}$  was superfused at a high rate (8–12 mL.min<sup>-1</sup>) with a modified oocyte Ringer's solution made of HEPES 5 mM pH 7.4,

NaCl 100 mM, KCl 2.8 mM, and BaCl<sub>2</sub> 0.3 mM, where BaCl<sub>2</sub> substitution to the original CaCl<sub>2</sub> prevents secondary activation of a Ca<sup>2+</sup>-dependent Cl<sup>-</sup> current [103]. Oocytes were first incubated for 45 s with the spiroimine to be assayed, and then ACh was applied for 5, 15, or 30 s using a computer-controlled multi-valve perfusion system (VC-6, Warner Instruments). To enable full receptor recovery from desensitization between successive ACh applications, 3-min perfusion intervals with the modified Ringer's solution were used.

Automated TEVC on  $\alpha 7$  and  $\alpha 4\beta 2$  nAChR oocytes was performed using a HiClamp system (Multi Channel Systems, GmbH., Reutlingen, Germany) [104]. Oocytes free of follicular cells were transferred from the 96-wells of the oocyte microplate to a recording basket carrying the reference bath electrode. Oocytes were automatically impaled and clamped at a holding potential of  $-60$  mV using borosilicate glass microelectrodes of 0.5–5 M $\Omega$  tip resistances, filled with a 1:1 (*v/v*) mixture of KCl 1 M and KAc 1 M. The clamped oocytes were exposed twice or thrice to ACh by incubation into a well containing ACh (at the EC<sub>50</sub> for the assayed nAChR subtype) to obtain a control IACH peak amplitude. Then, the oocytes were incubated with a given spiroimine alone for 45 s to test for a direct agonist effect, followed by immediate incubation with an ACh/spiroimine mixture. Finally, the clamped oocyte was moved to a washing well containing oocyte Ringer's solution for 30 s prior to its transfer to the washing station for 3 min.

## Appendix D.

### Appendix D.1. Stable Expression and Purification of the AChBPs

A- and L-AChBP, flanked with an N-terminal FLAG epitope with residues numbered (-8)DYKDDDDKL(0), were expressed as soluble, exported proteins using synthetic cDNA and stably-transfected HEK293S-GnTI<sup>-</sup> cells selected for G418 resistance [67], and cultured in Dulbecco's modified Eagle's medium (MediaTech CellGro, Albany, NY, USA) containing fetal bovine serum (FBS) 2% (*v/v*). The conditioned medium was collected every 1–3 days for up to 4 weeks, supplemented with NaN<sub>3</sub> 0.02% (*w/v*) and stored at 4 °C. AChBPs were purified on immobilized anti-FLAG M2 antibody (Sigma-Aldrich) with elution using FLAG peptide 100  $\mu$ g/mL in TRIS-HCl 50 mM pH 7.4, NaCl 150 mM, NaN<sub>3</sub> 0.02% (*w/v*) [64]. Purified proteins were dialyzed against the same buffer, concentrated by ultrafiltration, filtered on a 0.22  $\mu$ m membrane, and stored on ice at 4 °C.

### Appendix D.2. Formation and Crystallization of the Spiroimine-AChBP Complexes and Data Collection

The complexes were formed using ca. 240–320  $\mu$ M in A-AChBP subunit (ca. 6–8 mg/mL) and a 3-fold molar excess of the ( $\pm$ )-**4** racemate and purified (–)-**4 S** enantiomer or a 1.5-fold molar excess of the purified (+)-**4 R** enantiomer (incubation: 1 h at room temperature, then overnight at 4 °C). Crystallization was achieved manually by vapor diffusion at 18 °C using 1  $\mu$ L hanging drops and a 1:1 (*v/v*) protein-to-well solution ratio with the following well solutions: for the ( $\pm$ )-**4** racemate, PEG-1500 10% (*w/v*), sodium citrate 100 mM pH 5.5, NaCl 100 mM, isopropanol 24% (*v/v*); for spiroimine (+)-**4 R**, PEG-4K 17% (*w/v*), TRIS-HCl 100 mM pH 7.5, sodium citrate 200 mM pH 6.0, glycerol 10% (*v/v*); and for spiroimine (–)-**4 S**, PEG-4K 15% (*w/v*), HEPES 100 mM pH 7.5, isopropanol 10% (*v/v*), glycerol 10% (*v/v*). Crystals were rapidly soaked in the well solution complemented with 20% glycerol and flash-cooled in liquid nitrogen. Diffraction data for the racemic ( $\pm$ )-**4** and spiroimine (+)-**4 R** complexes were collected at beamlines ID23-1 and ID14-EH1 of the European Synchrotron Radiation Facility (Grenoble, France), respectively, while those for the spiroimine (–)-**4 S** complex were collected at beamline Proxima1 of the SOLEIL synchrotron (Gif-sur-Yvette, France). Data were integrated with XDS [105] and scaled and merged using the CCP4 suite [106] of programs POINTLESS [107], AIMLESS [108], and TRUNCATE [109]. Random sets of 5% of reflections were set aside for R<sub>free</sub> cross-validation purposes.



## References

1. Davidson, K.; Baker, C.; Higgins, C.; Higman, W.; Swan, S.; Veszelovszki, A.; Turner, A.D. Potential threats posed by new or emerging marine biotoxins in UK waters and examination of detection methodologies used for their control: Cyclic imines. *Mar. Drugs* **2015**, *13*, 7087–7112. [[CrossRef](#)] [[PubMed](#)]
2. Stivala, C.E.; Benoit, E.; Araújo, R.; Servent, D.; Novikov, A.; Molgó, J.; Zakarian, A. Synthesis and biology of cyclic imine toxins, an emerging class of potent, globally distributed marine toxins. *Nat. Prod. Rep.* **2015**, *32*, 411–435. [[CrossRef](#)] [[PubMed](#)]
3. Molgó, J.; Marchot, P.; Araújo, R.; Benoit, E.; Iorga, B.I.; Zakarian, A.; Taylor, P.; Bourne, Y.; Servent, D. Cyclic imine toxins from dinoflagellates: A growing family of potent antagonists of the nicotinic acetylcholine receptors. *J. Neurochem.* **2017**, *142* (Suppl. S2), 41–51. [[CrossRef](#)] [[PubMed](#)]
4. Farabegoli, F.; Blanco, L.; Rodríguez, L.P.; Vieites, J.M.; Cabado, A.G. Phycotoxins in marine shellfish: Origin, occurrence and effects on humans. *Mar. Drugs* **2018**, *16*, 188. [[CrossRef](#)] [[PubMed](#)]
5. Kim, Y.S.; An, H.J.; Kim, J.; Jeon, Y.J. Current situation of palytoxins and cyclic imines in Asia-pacific countries: Causative phytoplankton species and seafood poisoning. *Int. J. Environ. Res. Public Health* **2022**, *19*, 4921. [[CrossRef](#)] [[PubMed](#)]
6. Aasen, J.A.B.; Hardstaff, W.; Aune, T.; Quilliam, M.A. Discovery of fatty acid ester metabolites of spirolide toxins in mussels from Norway using liquid chromatography/tandem mass spectrometry. *Rapid Commun. Mass Spectrom.* **2006**, *20*, 1531–1537. [[CrossRef](#)] [[PubMed](#)]
7. McCarron, P.; Rourke, W.A.; Hardstaff, W.; Pooley, B.; Quilliam, M.A. Identification of pinnatoxins and discovery of their fatty acid ester metabolites in mussels (*Mytilus edulis*) from eastern Canada. *J. Agric. Food Chem.* **2012**, *60*, 1437–1746. [[CrossRef](#)] [[PubMed](#)]
8. De la Iglesia, P.; McCarron, P.; Diogène, J.; Quilliam, M.A. Discovery of gymnodimine fatty acid ester metabolites in shellfish using liquid chromatography/mass spectrometry. *Rapid Commun. Mass Spectrom.* **2013**, *27*, 643–653. [[CrossRef](#)]
9. Araújo, R.; Barnes, P.; Séchet, V.; Delepierre, M.; Zinn-Justin, S.; Molgó, J.; Zakarian, A.; Hess, P.; Servent, D. Cyclic imine toxins survey in coastal European shellfish samples: Bioaccumulation and mode of action of 28-O-palmitoyl ester of pinnatoxin-G—First report of portimine-A bioaccumulation. *Harmful Algae* **2020**, *98*, 101887. [[CrossRef](#)]
10. Ji, Y.; Che, Y.; Wright, E.J.; McCarron, P.; Hess, P.; Li, A. Fatty acid ester metabolites of gymnodimine in shellfish collected from China and in mussels (*Mytilus galloprovincialis*) exposed to *Karenia selliformis*. *Harmful Algae* **2020**, *92*, 101774. [[CrossRef](#)]
11. Varriale, F.; Tartaglione, L.; Cinti, S.; Milandri, A.; Dall’Ara, S.; Calfapietra, A.; Dell’Aversano, C. Development of a data dependent acquisition-based approach for the identification of unknown fast-acting toxins and their ester metabolites. *Talanta* **2021**, *224*, 121842. [[CrossRef](#)] [[PubMed](#)]
12. Kvrđic, K.; Lesic, T.; Aysal, A.I.; Dzafic, N.; Pleadin, J. Cyclic imines in shellfish and ascidians in the northern Adriatic Sea. *Food Addit. Contam. Part B-Surveill.* **2020**, *14*, 12–22. [[CrossRef](#)]
13. Otero, P.; Silva, M. Emerging marine biotoxins in European waters: Potential risks and analytical challenges. *Mar. Drugs* **2022**, *20*, 199. [[CrossRef](#)] [[PubMed](#)]
14. Finch, S.C.; Harwood, D.T.; Boundy, M.J.; Selwood, A.I. A review of cyclic imines in shellfish: Worldwide occurrence, toxicity and assessment of the risk to consumers. *Mar. Drugs* **2024**, *22*, 129. [[CrossRef](#)] [[PubMed](#)]
15. Servent, D.; Malgorn, C.; Bernes, M.; Gil, S.; Simasotchi, C.; Hérard, A.S.; Delzescaux, T.; Thai, R.; Barbe, P.; Keck, M.; et al. First evidence that emerging pinnatoxin-G, a contaminant of shellfish, reaches the brain and crosses the placental barrier. *Sci. Total Environ.* **2021**, *790*, 148125. [[CrossRef](#)] [[PubMed](#)]
16. Seki, T.; Satake, M.; MacKenzie, L.; Kaspar, H.F.; Yasumoto, T. Gymnodimine, a new marine toxin of unprecedented structure isolated from New Zealand oysters and the dinoflagellate, *Gymnodinium* sp. *Tetrahedron Lett.* **1995**, *36*, 7093–7096. [[CrossRef](#)]
17. Miles, C.O.; Wilkins, A.L.; Stirling, D.J.; MacKenzie, A.L. New analogue of gymnodimine from a *gymnodinium* species. *J. Agric. Food Chem.* **2000**, *48*, 1373–1376. [[CrossRef](#)]
18. Miles, C.O.; Wilkins, A.L.; Stirling, D.J.; MacKenzie, A.L. Gymnodimine C, an isomer of gymnodimine B, from *Karenia selliformis*. *J. Agric. Food Chem.* **2003**, *51*, 4838–4840. [[CrossRef](#)]
19. Haywood, A.J.; Steidinger, K.A.; Truby, E.W.; Bergquist, P.R.; Bergquist, P.L.; Adamson, J.; MacKenzie, L. Comparative morphology and molecular phylogenetic analysis of three new species of the genus *Karenia* (Dinophyceae) from New Zealand. *J. Phycol.* **2004**, *40*, 165–179. [[CrossRef](#)]
20. Tang, Z.; Qiu, J.; Wang, G.; Ji, Y.; Hess, P.; Li, A. Development of an efficient extraction method for harvesting gymnodimine-A from large-scale cultures of *Karenia selliformis*. *Toxins* **2021**, *13*, 793. [[CrossRef](#)]
21. Van Wagoner, R.M.; Misner, I.; Tomas, C.R.; Wright, J.L.C. Occurrence of 12-methylgymnodimine in a spirolide-producing dinoflagellate *Alexandrium peruvianum* and the biogenetic implications. *Tetrahedron Lett.* **2011**, *52*, 4243–4246. [[CrossRef](#)]
22. Van de Waal, D.B.; Tillmann, U.; Martens, H.; Krock, B.; van Scheppingen, Y.; John, U. Characterization of multiple isolates from an *Alexandrium ostenfeldii* bloom in The Netherlands. *Harmful Algae* **2015**, *49*, 94–104. [[CrossRef](#)]
23. Anttila, M.; Strangman, W.; York, R.; Tomas, C.; Wright, J.L. Biosynthetic studies of 13-desmethylspirolide C produced by *Alexandrium ostenfeldii* (= *A. peruvianum*): Rationalization of the biosynthetic pathway following incorporation of (13)C-labeled methionine and application of the odd-even rule of methylation. *J. Nat. Prod.* **2016**, *79*, 484–489. [[CrossRef](#)] [[PubMed](#)]
24. Harju, K.; Koskela, H.; Kremp, A.; Suikkanen, S.; de la Iglesia, P.; Miles, C.O.; Krock, B.; Vanninen, P. Identification of gymnodimine D and presence of gymnodimine variants in the dinoflagellate *Alexandrium ostenfeldii* from the Baltic Sea. *Toxicon* **2016**, *112*, 68–76. [[CrossRef](#)] [[PubMed](#)]

25. Martens, H.; Tillmann, U.; Harju, K.; Dell'Aversano, C.; Tartaglione, L.; Krock, B. Toxin variability estimations of 68 *Alexandrium ostenfeldii* (Dinophyceae) strains from The Netherlands reveal a novel abundant gymnodimine. *Microorganisms* **2017**, *5*, 29. [[CrossRef](#)]
26. Zurhelle, C.; Nieva, J.; Tillmann, U.; Harder, T.; Krock, B.; Tebben, J. Identification of novel gymnodimines and spirolides from the marine dinoflagellate *Alexandrium ostenfeldii*. *Mar. Drugs* **2018**, *16*, 446. [[CrossRef](#)]
27. Cembella, A.D.; Lewis, N.I.; Quilliam, M.A. The marine dinoflagellate *Alexandrium ostenfeldii* [Dinophyceae] as the causative organism of spirolide shellfish toxins. *Phycologia* **2000**, *39*, 67–74. [[CrossRef](#)]
28. Hu, T.; Burton, I.W.; Cembella, A.D.; Curtis, J.M.; Quilliam, M.A.; Walter, J.A.; Wright, J.L. Characterization of spirolides a, c, and 13-desmethyl c, new marine toxins isolated from toxic plankton and contaminated shellfish. *J. Nat. Prod.* **2001**, *64*, 308–312. [[CrossRef](#)]
29. Guéret, S.M.; Brimble, M.A. Spiroimine shellfish poisoning (SSP) and the spirolide family of shellfish toxins: Isolation, structure, biological activity and synthesis. *Nat. Prod. Rep.* **2010**, *27*, 1350–1366. [[CrossRef](#)]
30. Molgó, J.; Benoit, E.; Araújo, R.; Zakarian, A.; Iorga, B.I. Spirolides and cyclic imines: Toxicological profile. In *Marine and Freshwater Toxins*; Gopalakrishnakone, P., Haddad, V., Jr., Tubaro, A., Kim, E., Kem, W.R., Eds.; Springer: Dordrecht, The Netherlands, 2015; pp. 193–217. [[CrossRef](#)]
31. Nieva, J.A.; Tebben, J.; Tillmann, U.; Wohlrab, S.; Krock, B. Mass spectrometry-based characterization of new spirolides from *Alexandrium ostenfeldii* (Dinophyceae). *Mar. Drugs* **2020**, *18*, 505. [[CrossRef](#)]
32. Long, M.; Krock, B.; Castrec, J.; Tillmann, U. Unknown extracellular and bioactive metabolites of the genus *Alexandrium*: A review of overlooked toxins. *Toxins* **2021**, *13*, 905. [[CrossRef](#)] [[PubMed](#)]
33. Rhodes, L.; Smith, K.; Selwood, A.; McNabb, P.; van Ginkel, R.; Holland, P.; Munday, R. Production of pinnatoxins by a peridinoid dinoflagellate isolated from Northland, New Zealand. *Harmful Algae* **2010**, *9*, 384–389. [[CrossRef](#)]
34. Rhodes, L.; Smith, K.; Selwood, A.; McNabb, P.; Munday, R.; Suda, S.; Molenaar, S.; Hallegraef, G. Dinoflagellate *Vulcanodinium rugosum* identified as the causative organism of pinnatoxins in Australia, New Zealand and Japan. *Phycologia* **2011**, *50*, 624–628. [[CrossRef](#)] [[PubMed](#)]
35. Nézan, E.; Chomérat, N. *Vulcanodinium rugosum* gen. nov., sp. nov. (dinophyceae): A new marine dinoflagellate from the French Mediterranean coast. *Cryptogam. Algol.* **2011**, *32*, 3–18. [[CrossRef](#)]
36. Uemura, D.; Chou, T.; Haino, T.; Nagatsu, A.; Fukuzawa, S.; Zheng, S.Z.; Chen, H.S. Pinnatoxin-a—A toxic amphoteric macrocycle from the okinawan bivalve *Pinna muricata*. *J. Am. Chem. Soc.* **1995**, *117*, 1155–1156. [[CrossRef](#)]
37. Selwood, A.I.; Miles, C.O.; Wilkins, A.L.; van Ginkel, R.; Munday, R.; Rise, F.; McNabb, P. Isolation, structural determination and acute toxicity of pinnatoxins E, F and G. *J. Agric. Food Chem.* **2010**, *58*, 6532–6542. [[CrossRef](#)] [[PubMed](#)]
38. Selwood, A.I.; Wilkins, A.L.; Munday, R.; Gu, H.; Smith, K.F.; Rhodes, L.L.; Rise, F. Pinnatoxin H: A new pinnatoxin analogue from a South China Sea *Vulcanodinium rugosum* isolate. *Tetrahedron Lett.* **2014**, *55*, 5508–5510. [[CrossRef](#)]
39. Fribley, A.M.; Xi, Y.; Makris, C.; Alves-de-Souza, C.; York, R.; Tomas, C.; Wright, J.L.C.; Strangman, W.K. Identification of portimine B, a new cell permeable spiroimine that induces apoptosis in oral squamous cell carcinoma. *ACS Med. Chem. Lett.* **2018**, *10*, 175–179. [[CrossRef](#)] [[PubMed](#)]
40. Selwood, A.I.; Wilkins, A.L.; Munday, R.; Shi, F.; Rhodes, L.L.; Holland, P.T. Portimine: A bioactive metabolite from the benthic dinoflagellate *Vulcanodinium rugosum*. *Tetrahedron Lett.* **2013**, *4*, 4705–4707. [[CrossRef](#)]
41. Hermawan, I.; Higa, M.; Hutabarat, P.U.B.; Fujiwara, T.; Akiyama, K.; Kanamoto, A.; Haruyama, T.; Kobayashi, N.; Higashi, M.; Suda, S.; et al. Kabirimine, a new cyclic imine from an Okinawan dinoflagellate. *Mar. Drugs* **2019**, *17*, 353. [[CrossRef](#)]
42. Takada, N.; Umemura, N.; Suenaga, K.; Uemura, D. Structural determination of pteriatoxins A, B and C, extremely potent toxins from the bivalve *Pteria penguin*. *Tetrahedron Lett.* **2001**, *42*, 3495–3497. [[CrossRef](#)]
43. Hao, J.; Matsuura, F.; Kishi, Y.; Kita, M.; Uemura, D.; Asai, N.; Iwashita, T. Stereochemistry of pteriatoxins A, B, and C. *J. Am. Chem. Soc.* **2006**, *128*, 7742–7743. [[CrossRef](#)] [[PubMed](#)]
44. Torigoe, K.; Murata, M.; Yasumoto, T.; Iwashita, T. Prorocentrolide, a toxic nitrogenous macrocycle from a marine dinoflagellate, *Prorocentrum lima*. *J. Am. Chem. Soc.* **1988**, *110*, 7876–7877. [[CrossRef](#)]
45. Hu, T.; deFreitas, S.W.; Curtis, J.M.; Oshima, Y.; Walter, J.A.; Wright, J.L.C. Isolation and structure of prorocentrolide B, a fast-acting toxin from *Prorocentrum maculosum*. *J. Nat. Prod.* **1996**, *59*, 1010–1014. [[CrossRef](#)] [[PubMed](#)]
46. Amar, M.; Araújo, R.; Iorga, B.I.; Yasumoto, T.; Servent, D.; Molgó, J. Prorocentrolide-A from cultured *Prorocentrum lima* dinoflagellates collected in Japan blocks subtypes of nicotinic acetylcholine receptors. *Toxins* **2018**, *10*, 97. [[CrossRef](#)] [[PubMed](#)]
47. Lee, S.; Yang, A.R.; Yoo, Y.D.; Jeong, E.J.; Rho, J.R. Relative configurational assignment of 4-hydroxyprorocentrolide and prorocentrolide C isolated from a benthic dinoflagellate (*Prorocentrum lima*). *J. Nat. Prod.* **2019**, *82*, 1034–1039. [[CrossRef](#)] [[PubMed](#)]
48. Lu, C.-K.; Lee, G.-H.; Huang, R.; Chou, H.-N. Spiro-prorocentrimine, a novel macrocyclic lactone from a benthic *Prorocentrum* sp. of Taiwan. *Tetrahedron Lett.* **2001**, *42*, 1713–1716. [[CrossRef](#)]
49. Molgó, J.; Araújo, R.; Benoit, E.; Iorga, B. Cyclic imine toxins: Chemistry, origin, metabolism, pharmacology, toxicology and detection. In *Seafood and Freshwater Toxins: Pharmacology, Physiology and Detection*; Botana, L.M., Ed.; CRC Press: Boca Raton, FL, USA, 2014; pp. 951–989. [[CrossRef](#)]
50. Otero, A.; Chapela, M.J.; Atanassova, M.; Vieites, J.M.; Cabado, A.G. Cyclic imines: Chemistry and mechanism of action: A review. *Chem. Res. Toxicol.* **2011**, *24*, 1817–1829. [[CrossRef](#)] [[PubMed](#)]

51. Kasheverov, I.; Kudryavtsev, D.; Shelukhina, I.; Nikolaev, G.; Utkin, Y.; Tsetlin, V. Marine origin ligands of nicotinic receptors: Low molecular compounds, peptides and proteins for fundamental research and practical applications. *Biomolecules* **2022**, *12*, 189. [[CrossRef](#)]
52. Taylor, P. Agents acting at the neuromuscular junction and autonomic ganglia. In *Goodman and Gilman's The Pharmacological Basis of Therapeutics*; Brunton, L.L., Lazo, J.S., Parker, K.L., Eds.; McGraw-Hill: New York, NY, USA, 2006; pp. 217–236.
53. Changeux, J.P. The nicotinic acetylcholine receptor: The founding father of the pentameric ligand-gated ion channel superfamily. *J. Biol. Chem.* **2012**, *287*, 40207–40215. [[CrossRef](#)]
54. Le Novère, N.; Corringer, P.J.; Changeux, J.P. The diversity of subunit composition in nAChRs: Evolutionary origins, physiologic and pharmacologic consequences. *J. Neurobiol.* **2002**, *53*, 447–456. [[CrossRef](#)] [[PubMed](#)]
55. Gharpure, A.; Noviello, C.M.; Hibbs, R.E. Progress in nicotinic receptor structural biology. *Neuropharmacology* **2020**, *171*, 108086. [[CrossRef](#)]
56. Delgado-Vélez, M.; Quesada, O.; Villalobos-Santos, J.C.; Maldonado-Hernández, R.; Asmar-Rovira, G.; Stevens, R.C.; Lasalde-Dominicci, J.A. Pursuing high-resolution structures of nicotinic acetylcholine receptors: Lessons learned from five decades. *Molecules* **2021**, *26*, 5753. [[CrossRef](#)] [[PubMed](#)]
57. Unwin, N. Nicotinic acetylcholine receptor and the structural basis of neuromuscular transmission: Insights from *Torpedo* postsynaptic membranes. *Q. Rev. Biophys.* **2013**, *46*, 283–322. [[CrossRef](#)] [[PubMed](#)]
58. Changeux, J.P. The nicotinic acetylcholine receptor: A typical 'allosteric machine'. *Philos. Trans. R. Soc. Lond. B Biol. Sci.* **2018**, *373*, 20170174. [[CrossRef](#)] [[PubMed](#)]
59. Noviello, C.M.; Gharpure, A.; Mukhtasimova, N.; Cabuco, R.; Baxter, L.; Borek, D.; Sine, S.M.; Hibbs, R.E. Structure and gating mechanism of the  $\alpha 7$  nicotinic acetylcholine receptor. *Cell* **2021**, *184*, 2121–2134.e13. [[CrossRef](#)] [[PubMed](#)]
60. Morales-Perez, C.L.; Noviello, C.M.; Hibbs, R.E. X-ray structure of the human  $\alpha 4\beta 2$  nicotinic receptor. *Nature* **2016**, *538*, 411–415. [[CrossRef](#)]
61. Rahman, M.M.; Teng, J.; Worrell, B.T.; Noviello, C.M.; Lee, M.; Karlin, A.; Stowell, M.H.B.; Hibbs, R.E. Structure of the native muscle-type nicotinic receptor and inhibition by snake venom toxins. *Neuron* **2020**, *106*, 952–962.e5. [[CrossRef](#)]
62. Smit, A.B.; Syed, N.I.; Schaap, D.; van Minnen, J.; Klumperman, J.; Kits, K.S.; Lodder, H.; van der Schors, R.C.; van Elk, R.; Sorgedragger, B.; et al. A glia-derived acetylcholine-binding protein that modulates synaptic transmission. *Nature* **2001**, *411*, 261–268. [[CrossRef](#)]
63. Brejc, K.; van Dijk, W.J.; Klaassen, R.V.; Schuurmans, M.; van Der Oost, J.; Smit, A.B.; Sixma, T.K. Crystal structure of an ACh-binding protein reveals the ligand-binding domain of nicotinic receptors. *Nature* **2001**, *411*, 269–276. [[CrossRef](#)]
64. Hansen, S.B.; Talley, T.T.; Radić, Z.; Taylor, P. Structural and ligand recognition characteristics of an acetylcholine-binding protein from *Aplysia californica*. *J. Biol. Chem.* **2004**, *279*, 24197–24202. [[CrossRef](#)] [[PubMed](#)]
65. Celie, P.H.; van Rossum-Fikkert, S.E.; van Dijk, W.J.; Brejc, K.; Smit, A.B.; Sixma, T.K. Nicotine and carbamylcholine binding to nicotinic acetylcholine receptors as studied in AChBP crystal structures. *Neuron* **2004**, *41*, 907–914. [[CrossRef](#)] [[PubMed](#)]
66. Bourne, Y.; Talley, T.T.; Hansen, S.B.; Taylor, P.; Marchot, P. Crystal structure of a Cbtx-AChBP complex reveals essential interactions between snake alpha-neurotoxins and nicotinic receptors. *EMBO J.* **2005**, *24*, 1512–1522. [[CrossRef](#)] [[PubMed](#)]
67. Hansen, S.B.; Sulzenbacher, G.; Huxford, T.; Marchot, P.; Taylor, P.; Bourne, Y. Structures of *Aplysia* AChBP complexes with nicotinic agonists and antagonists reveal distinctive binding interfaces and conformations. *EMBO J.* **2005**, *24*, 3635–3646. [[CrossRef](#)] [[PubMed](#)]
68. Hibbs, R.E.; Sulzenbacher, G.; Shi, J.; Talley, T.T.; Conrod, S.; Kem, W.R.; Taylor, P.; Marchot, P.; Bourne, Y. Structural determinants for interaction of partial agonists with acetylcholine binding protein and neuronal alpha7 nicotinic acetylcholine receptor. *EMBO J.* **2009**, *28*, 3040–3051. [[CrossRef](#)] [[PubMed](#)]
69. Shahsavar, A.; Gajhede, M.; Kastrup, J.S.; Balle, T. Structural studies of nicotinic acetylcholine receptors: Using acetylcholine-binding protein as a structural surrogate. *Basic Clin. Pharmacol. Toxicol.* **2016**, *118*, 399–407. [[CrossRef](#)] [[PubMed](#)]
70. Camacho-Hernandez, G.A.; Taylor, P. Lessons from nature: Structural studies and drug design driven by a homologous surrogate from invertebrates, AChBP. *Neuropharmacology* **2020**, *179*, 108108. [[CrossRef](#)] [[PubMed](#)]
71. Bourne, Y.; Radić, Z.; Aráoz, R.; Talley, T.T.; Benoit, E.; Servent, D.; Taylor, P.; Molgó, J.; Marchot, P. Structural determinants in phycotoxins and AChBP conferring high affinity binding and nicotinic AChR antagonism. *Proc. Natl. Acad. Sci. USA* **2010**, *107*, 6076–6081. [[CrossRef](#)] [[PubMed](#)]
72. Bourne, Y.; Sulzenbacher, G.; Radić, Z.; Aráoz, R.; Reynaud, M.; Benoit, E.; Zakarian, A.; Servent, D.; Molgó, J.; Taylor, P.; et al. Marine macrocyclic imines, pinnatoxins A and G: Structural determinants and functional properties to distinguish neuronal  $\alpha 7$  from muscle  $\alpha 1(2)\beta\gamma\delta$  nAChRs. *Structure* **2015**, *23*, 1106–1115. [[CrossRef](#)]
73. Toumieux, S.; Beniazza, R.; Desvergnès, V.; Aráoz, R.; Molgó, J.; Landais, Y. Synthesis of the gymnodimine tetrahydrofuran core through a Ueno-Stork radical cyclization. *Org. Biomol. Chem.* **2011**, *9*, 3726–3732. [[CrossRef](#)]
74. Duroure, L.; Jousseau, T.; Aráoz, R.; Barré, E.; Retailleau, P.; Chabaud, L.; Molgó, J.; Guillou, C. 6,6-Spiroimine analogs of (–)-gymnodimine A: Synthesis and biological evaluation on nicotinic acetylcholine receptors. *Org. Biomol. Chem.* **2011**, *9*, 8112–8118. [[CrossRef](#)] [[PubMed](#)]
75. Alonso, E.; Otero, P.; Vale, C.; Alfonso, A.; Antelo, A.; Giménez-Llort, L.; Chabaud, L.; Guillou, C.; Botana, L.M. Benefit of 13-desmethyl spiroide C treatment in triple transgenic mouse model of Alzheimer disease: Beta-amyloid and neuronal markers improvement. *Curr. Alzheimer Res.* **2013**, *10*, 279–289. [[CrossRef](#)] [[PubMed](#)]

76. Hayashi, T.; Kanehira, K.; Hagihara, T.; Kumada, M.J. Asymmetric synthesis catalyzed by chiral ferrocenylphosphine-transition metal complexes. 5. Palladium-catalyzed asymmetric allylation of active methine compounds. *J. Org. Chem.* **1998**, *53*, 113–120. [CrossRef]
77. Hauser, T.A.; Hepler, C.D.; Kombo, D.C.; Grinevich, V.P.; Kiser, M.N.; Hooker, D.N.; Zhang, J.; Mountfort, D.; Selwood, A.; Akireddy, S.R.; et al. Comparison of acetylcholine receptor interactions of the marine toxins, 13-desmethylspirolide C and gymnodimine. *Neuropharmacology* **2012**, *62*, 2239–2250. [CrossRef]
78. Tan, K.P.; Singh, K.; Hazra, A.; Madhusudhan, M.S. Peptide bond planarity constrains hydrogen bond geometry and influences secondary structure conformations. *Curr. Res. Struct. Biol.* **2020**, *3*, 1–8. [CrossRef] [PubMed]
79. Bourne, Y.; Radić, Z.; Taylor, P.; Marchot, P. Conformational remodeling of femtomolar inhibitor-acetylcholinesterase complexes in the crystalline state. *J. Am. Chem. Soc.* **2010**, *132*, 18292–18300. [CrossRef] [PubMed]
80. Nemezc, Á.; Taylor, P. Creating an  $\alpha 7$  nicotinic acetylcholine recognition domain from the acetylcholine-binding protein: Crystallographic and ligand selectivity analyses. *J. Biol. Chem.* **2011**, *286*, 42555–42565. [CrossRef] [PubMed]
81. Kaczanowska, K.; Camacho Hernandez, G.A.; Bendiks, L.; Kohs, L.; Cornejo-Bravo, J.M.; Harel, M.; Finn, M.G.; Taylor, P. Substituted 2-aminopyrimidines selective for  $\alpha 7$ -nicotinic acetylcholine receptor activation and association with acetylcholine binding proteins. *J. Am. Chem. Soc.* **2017**, *139*, 3676–3684. [CrossRef] [PubMed]
82. Neudert, G.; Klebe, G. DSX: A knowledge-based scoring function for the assessment of protein-ligand complexes. *J. Chem. Inf. Model.* **2011**, *51*, 2731–2745. [CrossRef]
83. Rahman, M.M.; Basta, T.; Teng, J.; Lee, M.; Worrell, B.T.; Stowell, M.H.B.; Hibbs, R.E. Structural mechanism of muscle nicotinic receptor desensitization and block by curare. *Nat. Struct. Mol. Biol.* **2022**, *29*, 386–394. [CrossRef]
84. McCoy, A.J. Solving structures of protein complexes by molecular replacement with Phaser. *Acta Crystallogr. D Biol. Crystallogr.* **2007**, *63*, 32–41. [CrossRef] [PubMed]
85. Murshudov, G.N.; Vagin, A.A.; Dodson, E.J. Refinement of macromolecular structures by the maximum-likelihood method. *Acta Crystallogr. D Biol. Crystallogr.* **1997**, *53*, 240–255. [CrossRef] [PubMed]
86. Emsley, P.; Cowtan, K. Coot: Model-building tools for molecular graphics. *Acta Crystallogr. D Biol. Crystallogr.* **2004**, *60*, 2126–2132. [CrossRef] [PubMed]
87. CCP4. The CCP4 suite: Programs for protein crystallography. *Acta Crystallogr. D Biol. Crystallogr.* **1994**, *50*, 760–763. [CrossRef] [PubMed]
88. Krissinel, E.; Henrick, K. Inference of macromolecular assemblies from crystalline state. *J. Mol. Biol.* **2007**, *372*, 774–797. [CrossRef] [PubMed]
89. Davis, I.W.; Leaver-Fay, A.; Chen, V.B.; Block, J.N.; Kapral, G.J.; Wang, X.; Murray, L.W.; Arendall, W.B.; Snoeyink, J.; Richardson, J.S.; et al. MolProbity: All-atom contacts and structure validation for proteins and nucleic acids. *Nucleic Acids Res.* **2007**, *35*, W375–W383. [CrossRef] [PubMed]
90. Schrödinger, LLC. *The PyMOL Molecular Graphics System, Version 1.5.0.4*; Schrödinger, LLC: New York, NY, USA, 2010.
91. Robert, X.; Gouet, P. Deciphering key features in protein structures with the new ENDscript server. *Nucleic Acids Res.* **2014**, *42*, W320–W324. [CrossRef] [PubMed]
92. Taylor, P.; Shyong, Y.J.; Samskey, N.; Ho, K.Y.; Radić, Z.; Fenical, W.; Sharpless, K.B.; Kovarik, Z.; Camacho-Hernandez, G.A. Ligand design for human acetylcholinesterase and nicotinic acetylcholine receptors, extending beyond the conventional and canonical. *J. Neurochem.* **2021**, *158*, 1217–1222. [CrossRef] [PubMed]
93. Kem, W.R.; Andrud, K.; Bruno, G.; Xing, H.; Soti, F.; Talley, T.T.; Taylor, P. Interactions of nereistoxin and its analogs with vertebrate nicotinic acetylcholine receptors and molluscan ACh binding proteins. *Mar. Drugs* **2022**, *20*, 49. [CrossRef]
94. Sine, S.M.; Taylor, P. Relationship between reversible antagonist occupancy and the functional capacity of the acetylcholine receptor. *J. Biol. Chem.* **1981**, *56*, 6692–6699. [CrossRef]
95. Bouzat, C. New insights into the structural bases of activation of Cys-loop receptors. *J. Physiol. Paris* **2012**, *106*, 23–33. [CrossRef] [PubMed]
96. Dumont, J.N. Oogenesis in *Xenopus laevis* (Daudin). I. Stages of oocyte development in laboratory maintained animals. *J. Morphol.* **1972**, *136*, 153–179. [CrossRef] [PubMed]
97. Villeneuve, P.; Esnault, G.; Benoit, E.; Molgó, J.; Aráoz, R. A monitoring study of repetitive surgical oocyte harvest in *Xenopus laevis*. In *Toxins and Ion Transfers*; Collection Meetings in Toxinology; Barbier, J., Benoit, E., Gilles, N., Ladant, D., Martin-Eauclaire, M.F., Mattei, C., Molgó, J., Popoff, M.R., Servent, D., Eds.; SFET Publication: Gif-sur-Yvette, France, 2011; pp. 173–178. ISSN 1760-6004. Available online: <http://sfet.asso.fr/international/e-book-rt/e-book-rt.html> (accessed on 27 November 2011).
98. Kharrat, R.; Servent, D.; Girard, E.; Ouanounou, G.; Amar, M.; Marrouchi, R.; Benoit, E.; Molgó, J. The marine phycotoxin gymnodimine targets muscular and neuronal nicotinic acetylcholine receptor subtypes with high affinity. *J. Neurochem.* **2008**, *107*, 952–963. [CrossRef] [PubMed]
99. Krieger, F.; Mourot, A.; Aráoz, R.; Kotzyba-Hibert, F.; Molgó, J.; Bamberg, E.; Goeldner, M. Fluorescent agonists for the *Torpedo* nicotinic acetylcholine receptor. *ChemBioChem* **2008**, *9*, 1146–1153. [CrossRef] [PubMed]
100. Aráoz, R.; Ouanounou, G.; Iorga, B.I.; Goudet, A.; Alili, D.; Amar, M.; Benoit, E.; Molgó, J.; Servent, D. The neurotoxic effect of 13,19-didesmethyl and 13-desmethyl spirolide C phycotoxins is mainly mediated by nicotinic rather than muscarinic acetylcholine receptors. *Toxicol. Sci.* **2015**, *147*, 156–167. [CrossRef]

101. Miledi, R.; Palma, E.; Eusebi, F. Microtransplantation of neurotransmitter receptors from cells to *Xenopus* oocyte membranes: New procedure for ion channel studies. *Methods Mol. Biol.* **2006**, *322*, 347–355. [[CrossRef](#)]
102. Aráoz, R.; Servent, D.; Molgó, J.; Iorga, B.I.; Fruchart-Gaillard, C.; Benoit, E.; Gu, Z.; Stivala, C.; Zakarian, A. Total synthesis of pinnatoxins A and G, and revision of the mode of action of pinnatoxin A. *J. Am. Chem. Soc.* **2011**, *133*, 10499–10511. [[CrossRef](#)]
103. Sands, S.B.; Costa, A.C.; Patrick, J.W. Barium permeability of neuronal nicotinic receptor alpha 7 expressed in *Xenopus* oocytes. *Biophys. J.* **1993**, *65*, 2614–2621. [[CrossRef](#)] [[PubMed](#)]
104. Cieslikiewicz-Bouet, M.; Naldi, M.; Bartolini, M.; Pérez, B.; Servent, D.; Jean, L.; Aráoz, R.; Renard, P.-Y. Functional characterization of multifunctional ligands targeting acetylcholinesterase and alpha 7 nicotinic acetylcholine receptor. *Biochem. Pharmacol.* **2020**, *177*, 114010. [[CrossRef](#)]
105. Kabsch, W. XDS. *Acta Crystallogr. D Biol. Crystallogr.* **2010**, *66*, 125–132. [[CrossRef](#)]
106. Winn, M.D.; Ballard, C.C.; Cowtan, K.D.; Dodson, E.J.; Emsley, P.; Evans, P.R.; Keegan, R.M.; Krissinel, E.B.; Leslie, A.G.; McCoy, A.; et al. Overview of the CCP4 suite and current developments. *Acta Crystallogr. D Biol. Crystallogr.* **2011**, *67*, 235–242. [[CrossRef](#)] [[PubMed](#)]
107. Evans, P. Scaling and assessment of data quality. *Acta Crystallogr. D Biol. Crystallogr.* **2006**, *62*, 72–82. [[CrossRef](#)] [[PubMed](#)]
108. Evans, P.R.; Murshudov, G.N. How good are my data and what is the resolution? *Acta Crystallogr. D Biol. Crystallogr.* **2013**, *69*, 1204–1214. [[CrossRef](#)] [[PubMed](#)]
109. French, S.; Wilson, K. On the treatment of negative intensity observations. *Acta Crystallogr.* **1978**, *34*, 517–525. [[CrossRef](#)]

**Disclaimer/Publisher’s Note:** The statements, opinions and data contained in all publications are solely those of the individual author(s) and contributor(s) and not of MDPI and/or the editor(s). MDPI and/or the editor(s) disclaim responsibility for any injury to people or property resulting from any ideas, methods, instructions or products referred to in the content.

## Supplementary Material

# The Cyclic Imine Core Common to the Marine Macrocyclic Toxins Is Sufficient to Dictate Nicotinic Acetylcholine Receptor Antagonism

Yves Bourne <sup>1</sup>, Gerlind Sulzenbacher <sup>1</sup>, Laurent Chabaud <sup>2†</sup>, Rómulo Araújo <sup>3</sup>, Zoran Radić <sup>4</sup>, Sandrine Conrod <sup>5‡</sup>, Palmer Taylor <sup>4</sup>, Catherine Guillou <sup>2</sup>, Jordi Molgó <sup>3</sup>, Pascale Marchot <sup>1,5,\*</sup>

<sup>1</sup> Lab “Architecture et Fonction des Macromolécules Biologiques” (AFMB), Aix-Marseille Univ, CNRS, Faculté des Sciences Campus Luminy, 13288 Marseille cedex 09, France; yves.bourne@univ-amu.fr (Y.B.); gerlind.sulzenbacher@univ-amu.fr (G.S.)

<sup>2</sup> Institut de Chimie des Substances Naturelles (ICSN), Univ Paris-Saclay, CNRS, 91198 Gif-sur-Yvette, France; catherine.guillou@cnrs.fr

<sup>3</sup> Service d’Ingénierie Moléculaire pour la Santé (SIMoS) EMR CNRS 9004, Département Médicaments et Technologies pour la Santé, Institut des Sciences du Vivant Frédéric Joliot, CEA, INRAE, Université Paris-Saclay, 91191 Gif-sur-Yvette, France; romulo.araoz@cea.fr (R.A.); jordi.molgo@cea.fr (J.M.)

<sup>4</sup> Skaggs School of Pharmacy and Pharmaceutical Sciences (SSPPS), University of California San Diego, La Jolla, CA, 92093-0751, USA; zradic@health.ucsd.edu (Z.R.); pwtaylor@health.ucsd.edu (P.T.)

<sup>5</sup> Centre de Recherche en Neurobiologie et Neurophysiologie de Marseille (CRN2M), Aix Marseille Univ, CNRS, 13344 Marseille, France

† Current address: Institut des Sciences Moléculaires (ISM), Univ Bordeaux, CNRS, Bordeaux INP, 33400 Talence, France; laurent.chabaud@u-bordeaux.fr

‡ Current address: CEREGE, Aix-Marseille Univ, CNRS, IRD, Collège de France, INRAE, 13545 Aix-en-Provence, France; conrod@cerege.fr

\* Correspondence: pascale.marchot@univ-amu.fr

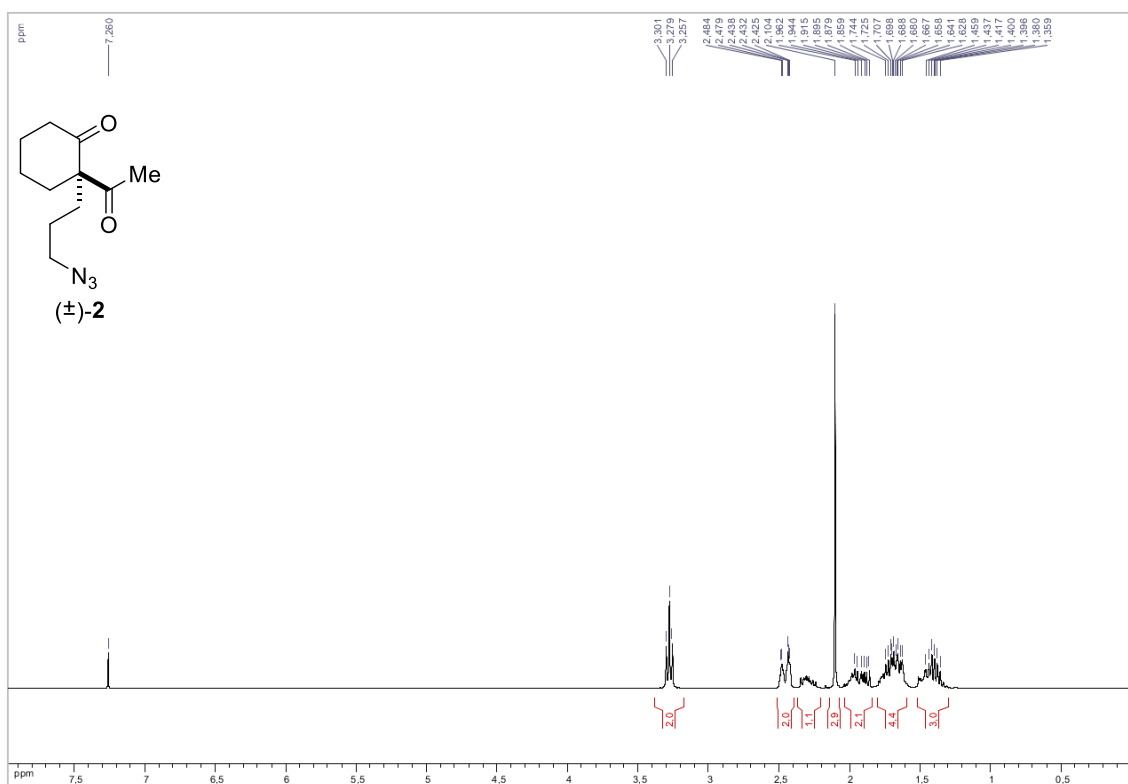


Figure S1. <sup>1</sup>H NMR spectrum (CDCl<sub>3</sub>) of 2-acetyl-2-(3-azidopropyl)cyclohexanone (±)-2.

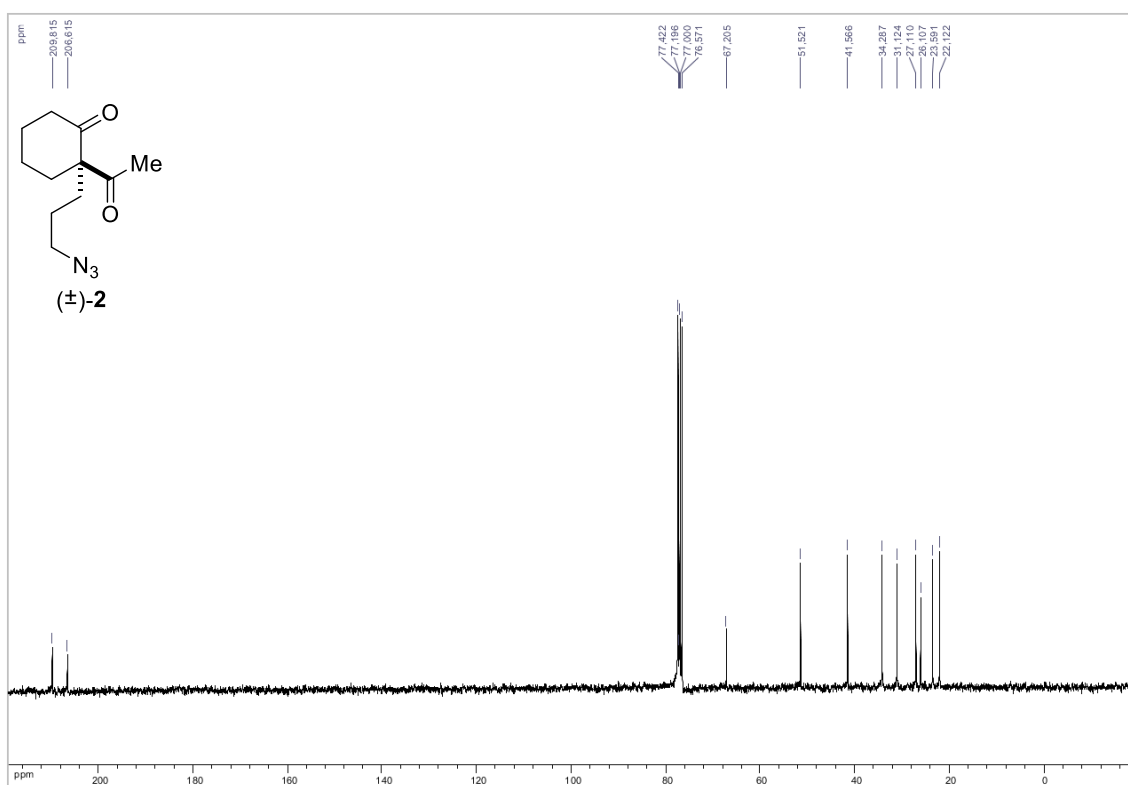
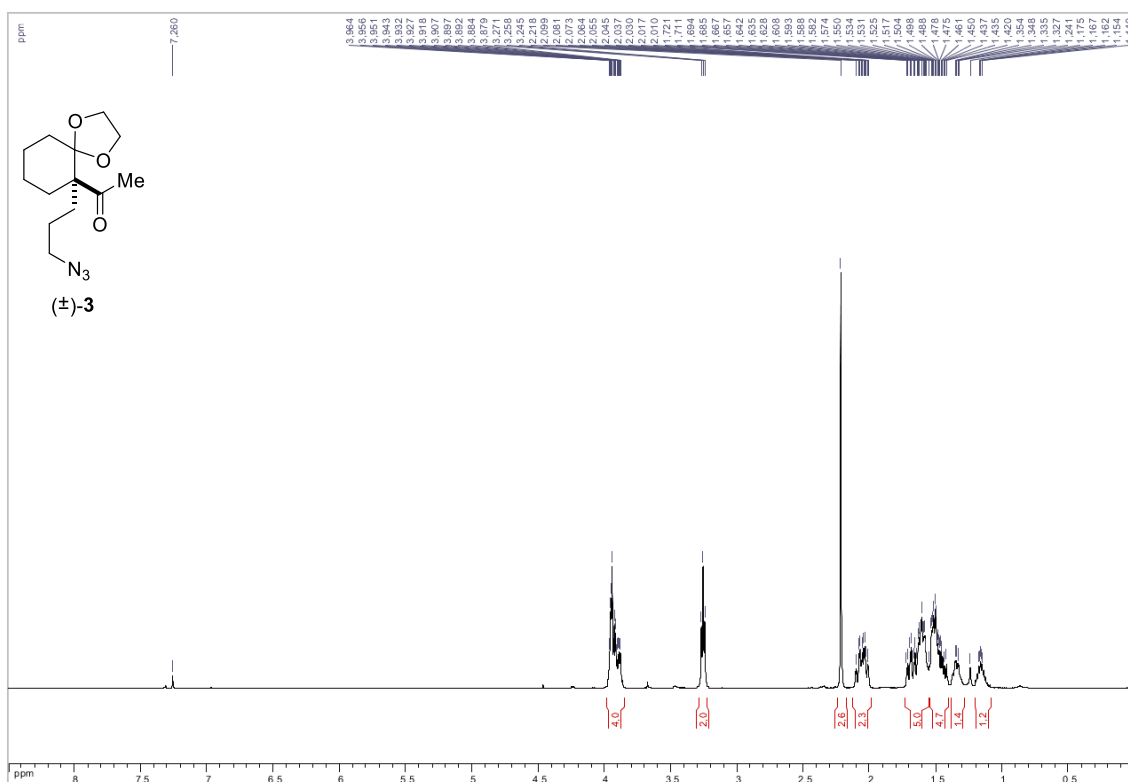
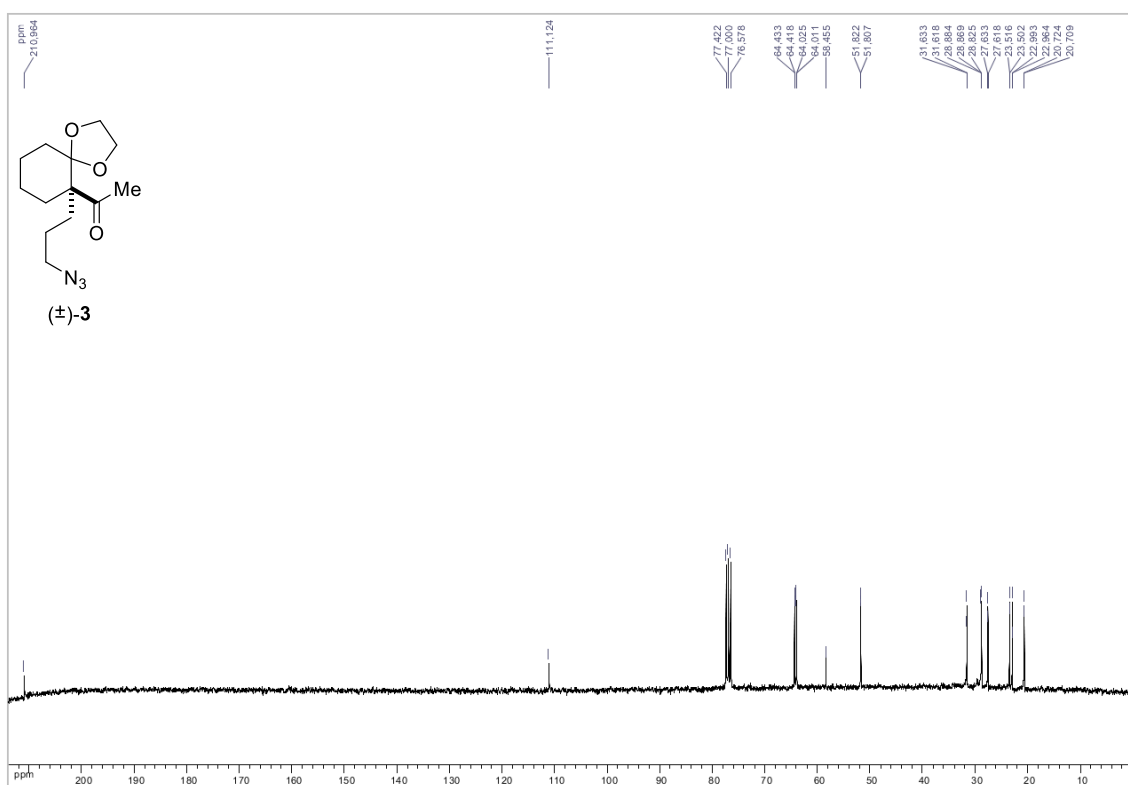


Figure S2. <sup>13</sup>C NMR spectrum (CDCl<sub>3</sub>) of 2-acetyl-2-(3-azidopropyl)cyclohexanone (±)-2.



**Figure S3.**  $^1\text{H}$  NMR spectrum ( $\text{CDCl}_3$ ) of 1-[6-(3-azidopropyl)-1,4-dioxaspiro[4.5]dec-6-yl]ethanone ( $\pm$ )-**3**.



**Figure S4.**  $^{13}\text{C}$  NMR spectrum ( $\text{CDCl}_3$ ) of 1-[6-(3-azidopropyl)-1,4-dioxaspiro[4.5]dec-6-yl]ethanone ( $\pm$ )-**3**.



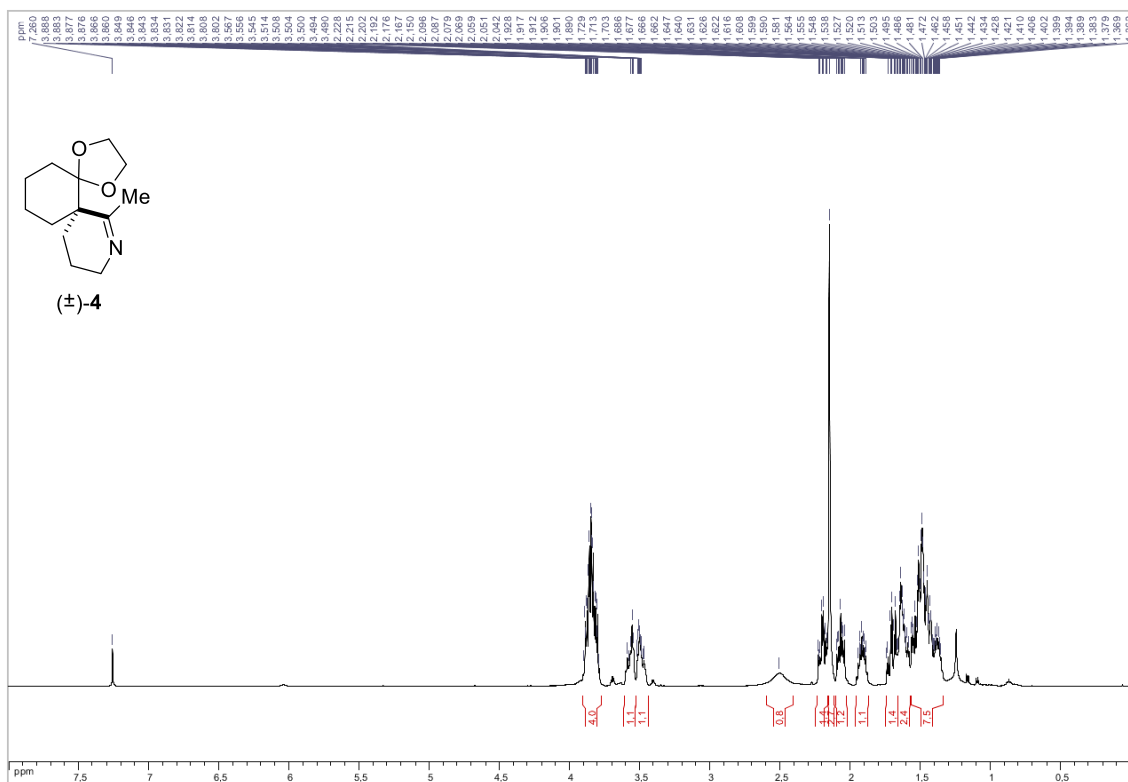


**Figure S5.**  $^1\text{H}$  NMR spectrum ( $\text{CDCl}_3$ ) of 7-methyl-1,4-dioxo-8-azadispiro[4.0.5.4]pentadec-7-ene ( $\pm$ )-4.

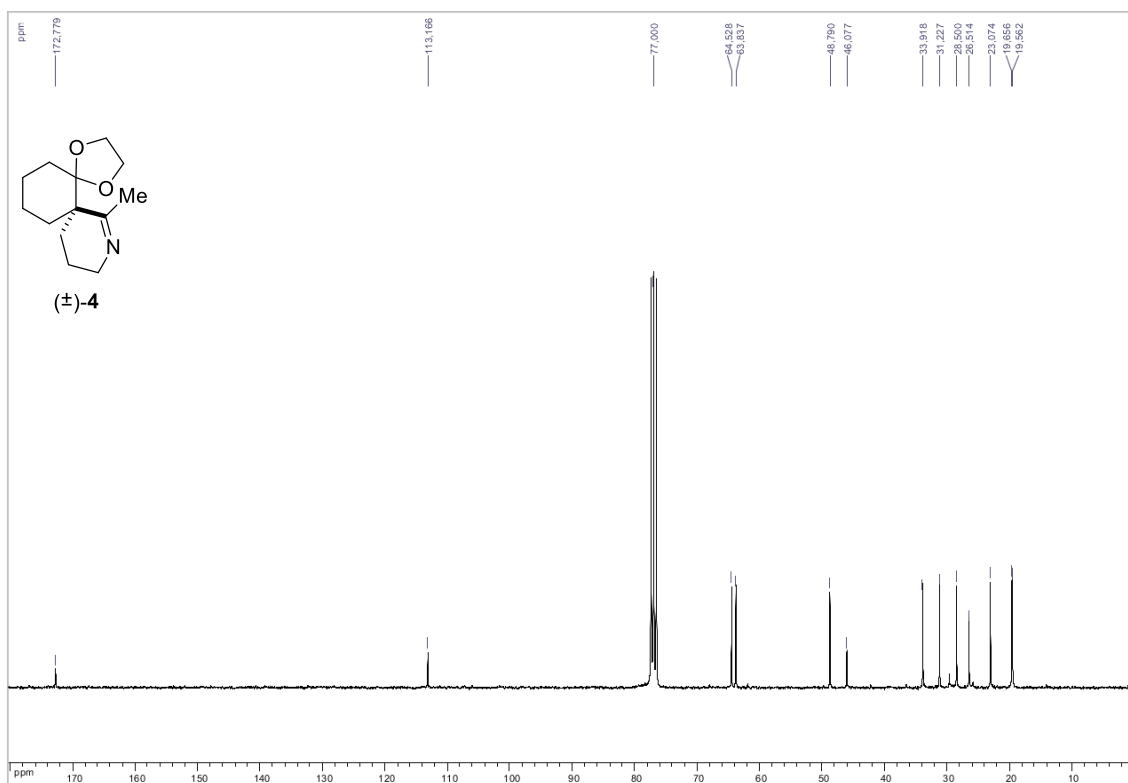


**Figure S6.**  $^{13}\text{C}$  NMR spectrum ( $\text{CDCl}_3$ ) of 7-methyl-1,4-dioxo-8-azadispiro[4.0.5.4]pentadec-7-ene ( $\pm$ )-4.

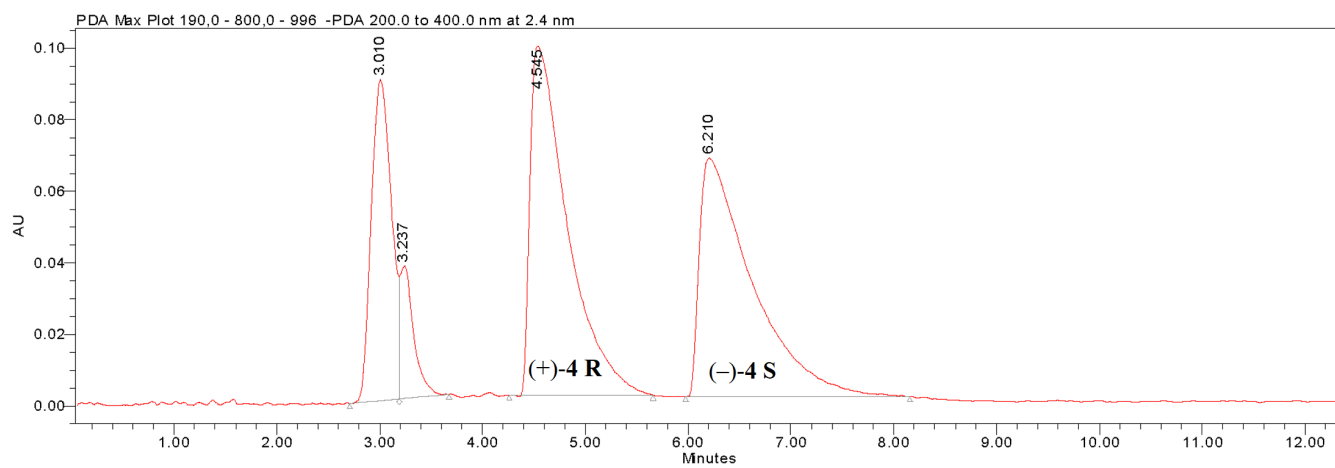


**Figure S7.** Separation of enantiomers (+)-4 and (-)-4 from the ( $\pm$ )-4 racemate using chiral HPLC (Chiralcel® OD 10  $\mu$ m 4.6x250 mm column, Hept/EtOH 80:20 (v/v), flow 1 mL/min).

**Table S1.** X-ray crystallography - Data collection and refinement statistics.

	Spiroimine (+)-4 R	Spiroimine (-)-4 S	Racemic (±)-4
Beamline	ESRF ID14-EH1	SOLEIL Proxima-1	ESRF ID23-1
<b>Data collection</b>			
Space group	P2 <sub>1</sub> 2 <sub>1</sub> 2 <sub>1</sub>	P2 <sub>1</sub> 2 <sub>1</sub> 2 <sub>1</sub>	P2 <sub>1</sub> 2 <sub>1</sub> 2 <sub>1</sub>
Cell dimensions <i>a</i> , <i>b</i> , <i>c</i> (Å)	87.98, 115, 129.96	88.34, 116.03, 131.04	75.79, 123.63, 131.1
Resolution <sup>a</sup> (Å)	48.13-2.00 (2.04-2.00)	48.49-1.85 (1.88-1.85)	65-2.10 (2.15-2.10)
No. reflections	89606 (4509)	109510 (5565)	72272 (4374)
CC (1/2)	0.999 (0.699)	1.0 (0.618)	0.993 (0.687)
<i>R</i> <sub>meas</sub> <sup>b</sup>	0.087 (0.959)	0.050 (0.954)	0.128 (0.720)
<i>I</i> / $\sigma$ <i>I</i>	15.5 (1.8)	22.2 (1.7)	8.7 (2.1)
Completeness (%)	100 (99.9)	94.9 (98.3)	99.7 (100)
Redundancy	6.2 (6.2)	7.0 (4.4)	3.5 (2.6)
Wilson B (Å <sup>2</sup> )	23.85	32.22	21.85
<b>Refinement</b>			
Resolution (Å)	48.18-2.00 (2.052-2.00)	47.97-1.85 (1.88-1.85)	65-2.1 (2.15-2.1)
No. reflections working set	84991 (6197)	103900 (7900)	70046 (5108)
No. reflections test set	4537 (317)	5509 (434)	2180 (148)
<i>R</i> <sub>work</sub> / <i>R</i> <sub>free</sub> <sup>c</sup>	0.1712/0.2060	0.1820/0.2114	0.18/0.21
No. atoms			
Protein + N-glycans	8457	8440	8560
Ligands/Ions	85	90	80
Water	784	706	520
B-factors			
Protein + N-glycans, main/side	32.92/38.29	38.67/43.39	33.7/38.5
Ligands/Ions	40	66.83	-
Water	37.38	42.06	36.4
R.m.s. deviations <sup>d</sup>			
Bond lengths (Å)	0.008	0.008	0.007
Bond angles (°)	1.472	1.447	1.271
Ramachandran			
Favoured (%)	98.94	99.04	98.5
Allowed (%)	1.06	0.96	1.5
Disallowed (%)	0	0	0
<i>PDB accession code</i>	8Q1M	8QTL	8QX2

<sup>a</sup> Values in parentheses are those for the highest-resolution shell. <sup>b</sup>  $R_{meas} = \frac{\sum_h \sum_i (n_h / (n_h - 1))^{1/2} |I_{hi} - \langle I_h \rangle|}{\sum_h \sum_i \langle I_h \rangle}$ , where *I* is an individual reflection measurement and  $\langle I \rangle$  is the mean intensity for symmetry-related reflections. <sup>c</sup>  $R_{work} = \frac{\sum_{hkl} ||F_o(hkl)| - |F_c||}{\sum_{hkl} |F_o(hkl)|}$ , where *F*<sub>o</sub> and *F*<sub>c</sub> are observed and calculated structure factors, respectively. *R*<sub>free</sub> is calculated for 5% of randomly selected reflections excluded from refinement. <sup>d</sup> Root-mean-square deviation from ideal values.

**Table S2.** Geometric parameters of key interactions between the (+)-4 R and (-)-4 S enantiomers and side chains in the A-AChBP binding pocket.

Subunit interface	Spiroimine (+)-4 R			Spiroimine (-)-4 S		
	Type of interaction			Type of interaction		
	H-bonds*	$\pi$ - $\pi$ stacking	van der Waals**	H-bonds*	$\pi$ - $\pi$ stacking	van der Waals**
A-B	N3-W147 carbonyl oxygen 2.6 Å / 140.7°	Cyclic imine- W147 face-to-face	Y93, Y188, C190, Y195 <i>Y55, I118,</i> <i>S167</i>	N3-W147 carbonyl oxygen 2.9 Å / 123.8°	Cyclic imine- W147 T-shaped	Y93, Y188, C190, C191, Y195 <i>Y55, I118</i>
B-C	N3-W147 carbonyl oxygen 2.7 Å / 144.2°	Cyclic imine- W147 face-to-face	Y93, Y188, C190, Y195 <i>Y55, I118</i>	N3-W147 carbonyl oxygen 3.5 Å / 121.2°	Cyclic imine- W147 T-shaped	Y93, Y188, C190, C191, Y195 <i>Y55, I118</i>
C-D	N3-W147 carbonyl oxygen 2.7 Å / 142°	Cyclic imine- W147 face-to-face	Y93, Y188, C190, Y195 <i>Y55, I118</i>	N3-W147 carbonyl oxygen 2.8 Å / 125.3°	Cyclic imine- W147 T-shaped	Y93, Y188, C190, C191, Y195 <i>Y55, I118</i>
D-E	N3-W147 carbonyl oxygen 2.7 Å / 144.4°	Cyclic imine- W147 face-to-face	Y93, Y188, C190, Y195 <i>Y55, I118</i>	N3-W147 carbonyl oxygen 3.0 Å / 126.9°	Cyclic imine- W147 T-shaped	Y93, Y188, C190, C191, Y195 <i>Y55, I118</i>
E-A	N3-W147 carbonyl oxygen 2.7 Å / 142.1°	Cyclic imine- W147 face-to-face	Y93, Y188, C190, Y195 <i>Y55, I118</i>	N3-W147 carbonyl oxygen 2.9 Å / 125.6°	Cyclic imine- W147 T-shaped	Y93, Y188, C190, C191, Y195 <i>Y55, I118</i>

\*The angle value refers to the  $\hat{H}$  angle between the hydrogen bond donor, acceptor and acceptor antecedent.

\*\*Non-italicized A-AChBP residues Y93, Y188, C190, C191, Y195 belong to the principal, (+) face of the subunit interface, while italicized residues *Y55, I118, S167* belong to the complementary, (-) face of the interface (Figure A1).

-----End of Suppl. Mat.-----